Topographic map formation and the effects of NMDA receptor blockade in the developing visual system

Vanessa J. Li[a], Anne Schohl[a], and Edward S. Ruthazer[a,1]

[a]Department of Neurology and Neurosurgery, Montreal Neurological Institute-Hospital, McGill University, Montréal, QC H3A 2B4, Canada

Edited by Carla Shatz, Department of Biology and Neurobiology, Stanford University, Stanford, CA; received April 26, 2021; accepted January 13, 2022

The development of functional topography in the developing brain follows a progression from initially coarse to more precisely organized maps. To examine the emergence of topographically organized maps in the retinotectal system, we performed longitudinal visual receptive field mapping by calcium imaging in the optic tectum of GCaMP6-expressing transgenic *Xenopus laevis* tadpoles. At stage 42, just 1 d after retinal axons arrived in the optic tectum, a clear retinotopic azimuth map was evident. Animals were imaged over the following week at stages 45 and 48, over which time the tectal neuropil nearly doubled in length and exhibited more precise retinotopic organization. By microinjecting GCaMP6s messenger ribonucleic acid (mRNA) into one blastomere of two-cell stage embryos, we acquired bilateral mosaic tadpoles with GCaMP6s expression in postsynaptic tectal neurons on one side of the animal and in retinal ganglion cell axons crossing to the tectum on the opposite side. Longitudinal observation of retinotopic map emergence revealed the presence of orderly representations of azimuth and elevation as early as stage 42, although presynaptic inputs exhibited relatively less topographic organization than the postsynaptic component for the azimuth axis. Retinotopic gradients in the tectum became smoother between stages 42 and 45. Blocking N-methyl-D-aspartate (NMDA) receptor conductance by rearing tadpoles in MK-801 did not prevent the emergence of retinotopic maps, but it produced more discontinuous topographic gradients and altered receptive field characteristics. These results provide evidence that current through NMDA receptors is dispensable for coarse topographic ordering of retinotectal inputs but does contribute to the fine-scale organization of the retinotectal projection.

Xenopus laevis | retinotectal | calcium imaging | activity dependent | mRNA microinjection

Topographic maps are a widespread phenomenon in vertebrate sensory circuits, well documented across multiple species and sensory modalities. Retinotopy in the visual system—the organized projection of retinal ganglion cells (RGCs) from the retina to the visual centers of the brain to form an orderly representation of the visual environment—is among the most well-studied examples of topographic sensory mapping (1–4), yet much remains to be unraveled regarding the process and underlying mechanisms of its emergence in early development.

The retinotopic map is first established by molecular guidance cues that direct RGC axons to topographically appropriate positions, establishing a coarse topographic gradient. Neuronal projections are further refined by patterned neural activity into more orderly and precise configurations (5–8). A challenge for studying the activity-dependent refinement process in higher vertebrate models is the difficulty of visualizing and manipulating the visual system in these early stages. In mammals, the refinement of the retinocollicular map is largely completed before the onset of visual experience, instructed by waves of spontaneous activity (9–11). In contrast, the retinotectal projections of fish and frogs rely directly on patterned visual experience for refinement (5, 12), opening many possibilities for experimental intervention. In particular, Xenopus develop externally from large oocytes, easily subject to pharmacological and genetic manipulation (13, 14). The transparent skin of albino Xenopus tadpoles further permits noninvasive in vivo imaging. These traits make Xenopus tadpoles an ideal model for studying the early development of topographic maps.

In the developing tadpole tectum, directing neuronal arbors to their appropriate topographic positions is not a static problem, as the tectum is continuously expanding and adding new cells throughout this process. A further level of complexity arises when considering the patterns by which new cells are added. The tadpole eye adds neurons radially at the peripheral margin of the retina (15), but the tadpole tectum adds new neurons linearly from its caudo-medial edge (16). In order to produce a uniform map, the connections between RGCs and postsynaptic tectal cells need to shift partners continuously, requiring a high degree of circuit plasticity.

The activity-dependent remodeling of the axonal and dendritic processes of individual neurons has been extensively described in Xenopus (8). However, most of these studies were performed on single neurons or small neuronal populations. To date, characterizations of the evolution of the full retinotectal map in Xenopus have only been done via anatomical tracing (17) or coarse multiunit electrophysiology recordings (18, 19). Therefore, in the present study, we aimed to take advantage

Significance

Studying the emergence of topographic organization in sensory maps has been constrained by spatial limitations of traditional anatomical and physiological techniques early in development in many animal models. Here, we have applied a high-resolution, noninvasive, in vivo calcium imaging approach to study the nascent retinotopic map in the larval *Xenopus laevis* retinotectal system. We performed longitudinal functional imaging of the three-dimensional organization of emerging retinotopic maps and assessed the effects of N-methyl-D-aspartate (NMDA) receptor blockade on map formation. Our results provide insights into early retinotopic map emergence and the role of NMDA receptors in the refinement of topographic gradients.

Author contributions: V.J.L., A.S., and E.S.R. designed research; V.J.L. and A.S. performed research; V.J.L. and A.S. contributed new reagents/analytic tools; V.J.L. and E.S.R. analyzed data; E.S.R. supervised the trainee; V.J.L. and E.S.R. wrote the paper; and A.S. edited the paper.

The authors declare no competing interest.

This article is a PNAS Direct Submission.

[1]To whom correspondence may be addressed. Email: edward.ruthazer@mcgill.ca.

This article contains supporting information online at http://www.pnas.org/lookup/suppl/doi:10.1073/pnas.2107899119/-/DCSupplemental.

Published February 22, 2022.

of multiphoton microscopy and genetically encoded calcium indicators to obtain a whole-circuit, fine-scale functional characterization of the nascent retinotopic map in Xenopus tadpoles. We further sought to repeatedly visualize presynaptic and postsynaptic maps independently over the initial period of map formation and development.

The N-methyl-D-aspartate (NMDA) receptor is considered a key player in neural circuit refinement, its activity having been shown to affect arbor morphology, branch stability, and synaptic plasticity (20–24). The segregation of retinal afferents into eye-specific bands in three-eyed frogs, thought to reflect the influence of differential patterned activity on axonal arborization, is prevented by blockers of NMDA receptors (25, 26). In both frog and mammalian systems, the retinotopic precision of RGC input convergence has been found to be degraded by tectal NMDA receptor blockade (27, 28). Given these results based primarily on anatomical reconstructions of individual or small groups of cells, we sought to assess the contributions of NMDA receptors to the development of the map at the whole-circuit level.

Results

Visualizing the Retinotopic Map in the Tadpole Tectum. The functional retinotopic map in the optic tectum of developing Xenopus tadpoles was studied by presenting visual mapping stimuli to transgenic Xenopus tadpoles expressing the genetically encoded calcium indicator GCaMP6s (29). Tadpoles were immobilized in agarose in an imaging chamber with a side window to permit viewing of a small liquid crystal display (LCD) video monitor placed next to the animal. The corresponding calcium responses were recorded from the contralateral optic tectum using a resonant scanning two-photon microscope (Fig. 1 *A* and *B*). GCaMP6s expression levels in the transgenic tadpoles were sufficient to detect visually evoked responses in the optic tectum in some animals as early as stage 42, as defined by Nieuwkoop and Faber (30).

Animals maintained an adequate level of fluorescence for up to a week after tadpoles had matured to stage 48. This provided a suitable time window for functional characterization of the initial emerging retinotopic map by calcium imaging.

Axonal inputs from RGCs ramify topographically in the tectal neuropil where they synapse upon the dendritic arborizations of postsynaptic tectal neurons (Fig. 1*C*). Thus, the organization of inputs is best reflected by the activity in the neuropil region of the tectum, where we carried out the majority of our receptive field map analyses. We devised two independent visual stimulation protocols to extract retinotopic maps: phase mapping and grid mapping. We compared maps independently extracted from the same animals using both methods, the results of which served to validate each other (*SI Appendix*, Fig. S1).

For phase mapping, we placed an LCD monitor in front of one eye of the tadpole and repeatedly presented a slow-moving dark vertical or horizontal bar that swept across the full span of the monitor every 20 s, with 10 s for the sweep, followed by 10 s pause. The tectal response to this stimulus was a transient wave of elevated GCaMP6s fluorescence intensity that swept across the optic tectum, the response waves occurring with the same periodicity as the sweeping bar (Fig. 1 *D–F* and Movie S1). We generated Fourier power spectra for the fluorescence time courses at each pixel and measured the phase of the response at the stimulus frequency for bars swept in both directions of the azimuth and elevation axes (31). This creates a phase map that represents the visual field positions that evoked maximal responses at each point in the tectum (Fig. 1*G* and *SI Appendix*, Figs. S1 and S2). Phase mapping is a highly sensitive method, which consistently and robustly revealed functional retinotopy in both the cell body layer and the neuropil.

For grid mapping, we randomly presented a stationary dark vertical or horizontal bar at each of five positions evenly spaced along either the azimuth or elevation axis of the visual field. At these early stages, most locations in the tectum responded to some extent for all five positions but with a preference for one of the positions (*SI Appendix*, Fig. S1). Therefore, for each pixel within the tectum, we calculated an "optimal stimulus position" by weighting the responses of that pixel to bars at each stimulus position. This value estimates the center of the visual field representation for the responsive pixel (Fig. 1 *H*, *Center*). Like phase maps, grid maps consistently revealed functional retinotopy in both the cell body and the neuropil layers, albeit showing an apparently smaller range of receptive field positions at the periphery, compared with phase maps from the same animal at roughly the same imaging depth.

In general, phase mapping and grid mapping methods produced retinotopic maps in GCaMP6s transgenic Xenopus tadpoles that broadly matched each other. We quantified pixelwise differences between phase maps and grid maps extracted from the neuropil zone of the same animals and found these differences to be significantly smaller on average than the mean difference between the phase map and its scrambled version, confirming that maps extracted through the two different methods were consistent with each other (*SI Appendix*, Fig. S1 *F* and *G*).

We also computed grid maps for the tectal cell somata by calculating optimal stimulus position for cell body regions-of-interest (ROIs) instead of single pixels, based on average $\Delta F/F_0$ calcium signal over all pixels within each ROI (Fig. 1 *H*, *Right*). The distribution of optimal stimulus positions in cell body ROIs appeared consistent with the topographic gradient of optimal stimulus positions in the corresponding neuropil region of the pixelwise grid map.

Changes in Retinotopic Maps over Development. To observe how the retinotopic map evolves during early development, we imaged GCaMP6s transgenic tadpoles at different developmental stages from stage 42 to stage 48 (Fig. 2*A*). We performed retinotopic mapping by applying the phase mapping method to multiple optical sections within a tectal volume to extract a three-dimensional (3D) representation of functional retinotopy (Fig. 2 and *SI Appendix*, Figs. S3 and S4). We were able to visualize maps in tadpoles as young as stage 42, shortly after the first arrival of RGC axons in the optic tectum, and then reimage the same animals repeatedly at later stages. Fig. 2 shows maps acquired from the same GCaMP6s transgenic animal at stages 42, 45, and 48 (Fig. 2 *B*, *D*, and *F*). When raised at 20 °C, tadpoles reach stage 42 roughly a week after fertilization; stages 42, 45, and 48 are separated by about 2 to 3 d each. We assembled 3D maps of the emerging visual field representations in the tectal neuropil at these stages (Fig. 2 *E* and *G*; *SI Appendix*, Figs. S3 *B* and *D* and S4 *B*, *D*, and *F*; and Movies S2–S5).

In transgenic tadpoles at stage 42, the tectal map already displayed a striking topographic gradient in the azimuth axis, while a gradient for elevation was less apparent (Fig. 2*B* and *SI Appendix*, Fig. S4). Over the course of development from stage 42 to 48, the tectal neuropil roughly doubled in length (Fig. 2*C*), and the topographic gradients became increasingly defined. At stage 45, a strong gradient in the azimuth map can be seen along the rostral–caudal axis of the tectum (Fig. 2 *D* and *E*), consistent with previous reports based on coarse multiunit electrophysiological and anatomical tracing (17, 19). At this stage, a robust gradient for the elevation axis within the 3D volume of the tadpole tectum is also evident. By stage 48, the azimuthal gradient within the 3D tectal volume has moved with respect to the rostrocaudal axis of the animal (Fig. 2 *F* and *G*). We projected the receptive field centers from the tectal neuropil onto the visual field and found that, despite changes in the map orientation within the tectum, the visual field represented in the

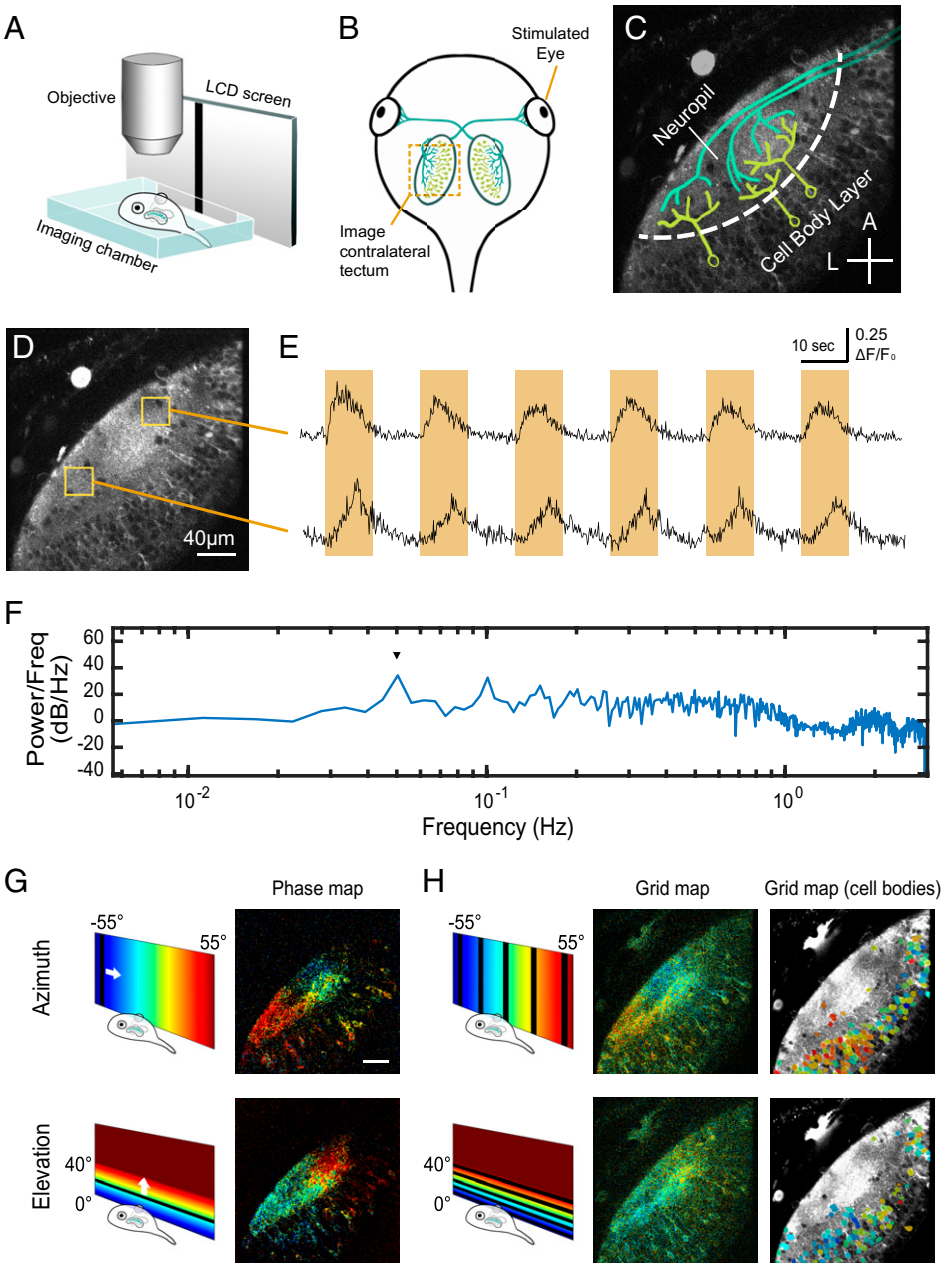

Fig. 1. Experiment setup for visualizing retinotopic maps in the tadpole tectum. (*A*) Schematic of imaging setup. The tadpole was immobilized and embedded in agarose in an imaging chamber under the microscope, with one eye viewing visual stimuli on an LCD screen through a glass slide on the side of the imaging chamber. (*B*) Schematic of the tadpole retinotectal system. RGC axons innervate the contralateral tectum. (*C*) Imaging field in the tadpole tectum corresponding to the region indicated in *B*, showing discrete neuropil and cell body layers. RGC axons are in green, and postsynaptic tectal neurons are in yellow. A, anterior; L, lateral. (Cross bars: 40 μm.) (*D*) Two-photon optical section in GCaMP6s transgenic tadpole tectum. (*E*) Mean GCaMP6s $\Delta F/F_0$ plots from the anterior and posterior tectal ROIs in *D* showing responses to an anterior to posterior drifting bar stimulus. Each cycle consisted of a bar slowly traversing the monitor once over 10 s followed by 10 s blank, thus repeating every 20 s. Orange highlights indicate when the drifting bar was visible. Signal in the anterior ROI peaked at an earlier time per sweep (phase) than in the posterior ROI. (*F*) Fourier power spectrum of the first differential of a calcium response to 10 repeats of the drifting bar stimulus measured over the neuropil (single optical section, 6-Hz acquisition rate). A peak in power (arrowhead) occurs at the stimulus frequency (0.05 Hz). (*G*) Examples of retinotopic maps extracted from a stage 48 transgenic animal color coded by phase of response to drifting bar stimuli. Pixel brightness in phase maps indicates SNR. (*H*) "Grid maps" were obtained by flashing a bar at five locations across azimuth or elevation. (*Center*) Pixelwise grid maps obtained from the same animal in *G* color coded by optimal stimulus position. Pixel brightness reflects the maximal evoked response ($\Delta F/F_0$) divided by the mean of evoked responses to the dark bar stimuli. (*Right*) Cell body grid maps from the same animal. Cell body ROIs are color coded by optimal stimulus position and overlaid on a time-averaged image of the tectum. (Scale bars: 40 μm.)

tectum remained relatively consistent between stage 45 and stage 48, with lower-elevation receptive fields more densely represented in the tecta at both stages (Fig. 2 *H* and *I*).

An interesting observation was that the orientation of the retinotopic map appeared to undergo an axis rotation in Cartesian coordinates between stages 45 and 48. To estimate the map axes in three dimensions, we calculated the "global topographic gradient" vectors for the azimuth and elevation maps by summing the local gradient vectors in the neuropil, calculated for each pixel as the differences in topographic position (phase) from adjacent pixels in the *x*, *y*, and *z* directions (*SI Appendix*, Fig. S5). Both the azimuth and elevation gradient axes seemed

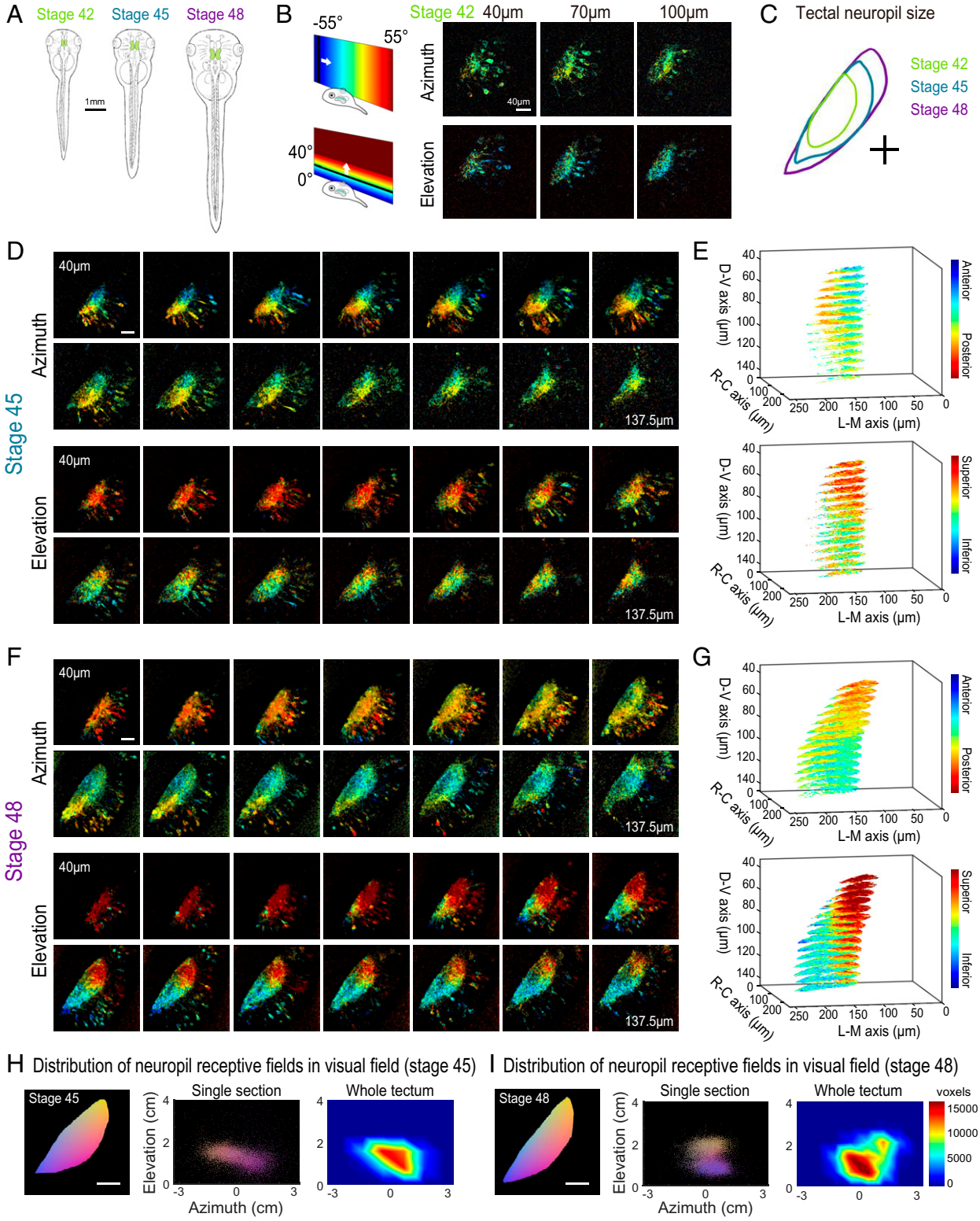

Fig. 2. Retinotopic map over different developmental stages. (*A*) Sketches of an *X. laevis* tadpole at stages 42, 45, and 48. (*B*) Phase maps extracted from a stage 42 GCaMP6s-expressing transgenic tadpole at three depths. (*C*) Comparison of tectal neuropil outlines traced from two-photon images of the same animal at stages 42, 45, and 48 (depth is ~100 μm from the top of tectum). (*D*) Phase maps extracted from the same tadpole at stage 45. For both azimuth and elevation, a stack of 14 optical sections is shown (40 to 135.75 μm from the top surface of the tectum, 7.5 μm between optical sections). Pixel intensities indicate SNR. (*E*) 3D volume rendering of phase maps from *D*. D-V is dorsoventral. R-C is rostrocaudal. L-M is lateromedial. (*F*) Phase maps extracted from the same tadpole at stage 48. Stack of 14 optical sections. (*G*) Phase maps from *F* rendered as a 3D volume. In *E* and *G*, only pixels in the neuropil region with SNR > 1.5 are shown. (*H* and *I*) Tectal neuropil positions from an optical section at 100-μm depth (*Left*) mapped onto the stimulus display area (6.5 × 4 cm; *Center*) for the tadpole at (*H*) stage 45 and (*I*) stage 48. Colors represent tectal neuropil coordinates (*Left* and *Center*). Density plots (*Right*) show the distribution of neuropil receptive fields from the whole tectum mapped onto the stimulus display area (summed from 14 optical sections, 7.5 μm between slices). (Scale bars: *A*, 1 mm; *B*–*I*, 40 μm.)

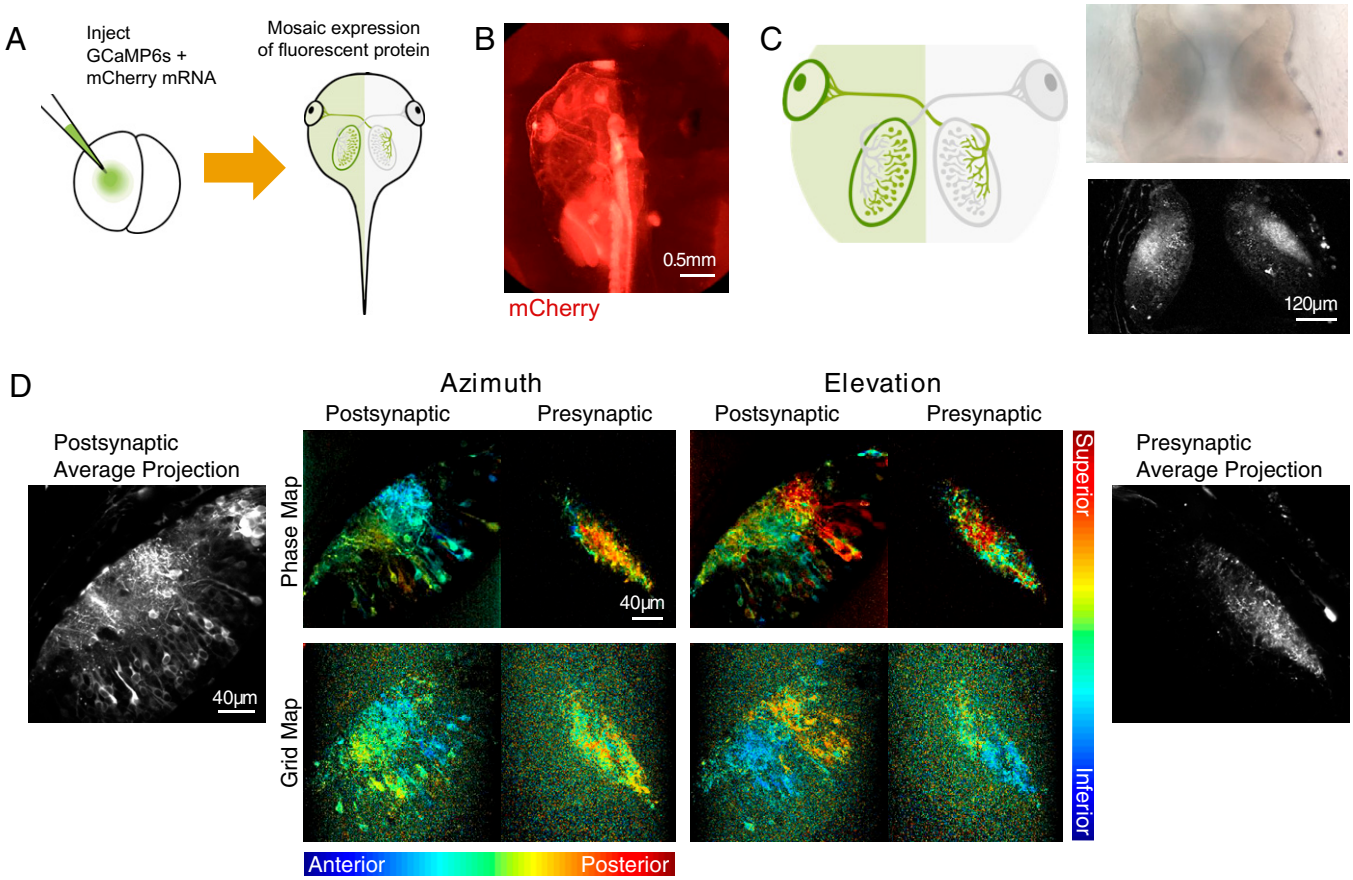

Fig. 3. GCaMP mosaic post- and presynaptic expression in tectum. (*A*) Schematic of mRNA injection of two-cell stage embryos. Injecting GCaMP6s and mCherry mRNA into one blastomere of two-cell stage tadpole embryos results in mosaic expression of fluorescent protein restricted to one-half of the body. (*B*) Epifluorescence image of mCherry expression restricted to the left half of the tadpole. mCherry was used to confirm half-animal mosaic expression of fluorescent proteins. (*C*) Schematic showing restriction of GCaMP expression to post- and presynaptic compartments in the left and right hemispheres, respectively. Transmitted light image (*Upper Right*) and two-photon optical section (*Lower Right*) of post- and presynaptic GCaMP expression in the two tectal hemispheres. (*D*) Phase maps (*Upper Center*) and grid maps (*Lower Center*) extracted from the left and right tectal hemispheres in the same GCaMP6s mRNA hemi-mosaic animal. For phase maps, pixel brightness indicates SNR. For grid maps, pixel brightness reflects the maximal evoked response ($\Delta F/F_0$) divided by the mean of all evoked responses. Time-averaged images of post- and presynaptic GCaMP expression are shown in *Left* and *Right*.

to undergo noticeable changes in orientation between stages 45 and 48. The azimuth gradient initially was nearly aligned with the rostrocaudal axis of the tadpole but shifted toward a more dorsoventral orientation at stage 48, while the elevation gradient shifted from a predominantly dorsoventral orientation toward slightly greater mediolateral axis alignment (*SI Appendix*, Table S1). This observed change may in part be a result of tectal growth between the two stages, displacing previously imaged tectal volumes into different planes of section. Furthermore, the angle between the azimuth and elevation gradient axes became slightly more orthogonal at stage 48 (*SI Appendix*, Fig. S5 *B* and *D*).

Comparing the Retinotopic Maps in Presynaptic and Postsynaptic Compartments of the Tectum. To observe the emergence of the retinotopic map in the presynaptic (RGC axons) and postsynaptic (tectal neurons) components of the retinotectal circuit, we took advantage of the ability to drive GCaMP expression in one-half of the tadpole (Fig. 3). Injecting GCaMP6s mRNA into one blastomere of two cell–stage embryos creates animals with mosaic fluorescent protein expression, which in some cases, is restricted to exactly one lateral half of the animal (Fig. 3*A*). mCherry mRNA was coinjected with GCaMP6s to aid in visualizing the distribution of fluorescent protein (Fig. 3*B*). Because the retinotectal projection is entirely crossed at this developmental stage, these hemi-mosaic tadpoles will have expression restricted exclusively to the postsynaptic tectal cells on the labeled side and the presynaptic RGC axon terminals within the opposite tectal hemisphere (Fig. 3*C*). In mRNA animals, we obtained clear retinotopic maps with both phase and grid mapping methods in both RGC axon terminals and postsynaptic tectal cells (Fig. 3*D*). We found that overall GCaMP6s signal strength and signal-to-noise ratio (SNR) were significantly higher in postsynaptic compared with presynaptic compartments (*SI Appendix*, Fig. S6). The period of GCaMP expression was similar in transgenic and mRNA-injected animals, with GCaMP fluorescence persisting for up to a week after tadpoles reached stage 48, before declining in both cases to levels suboptimal for analysis.

Longitudinal Imaging of Post- and Presynaptic Topographic Map Development. We followed the development of retinotopic maps in both the axonal and dendritic compartments over time in the same hemi-mosaic animals, reconstructing 3D functional map volumes at stages 42, 45, and 48 (Fig. 4*A*; *SI Appendix*, Figs. S7–S9; and Movies S6–S9). Topographic maps were present at all three stages imaged, and postsynaptic gradients for the azimuthal visual axis in particular were strikingly evident in

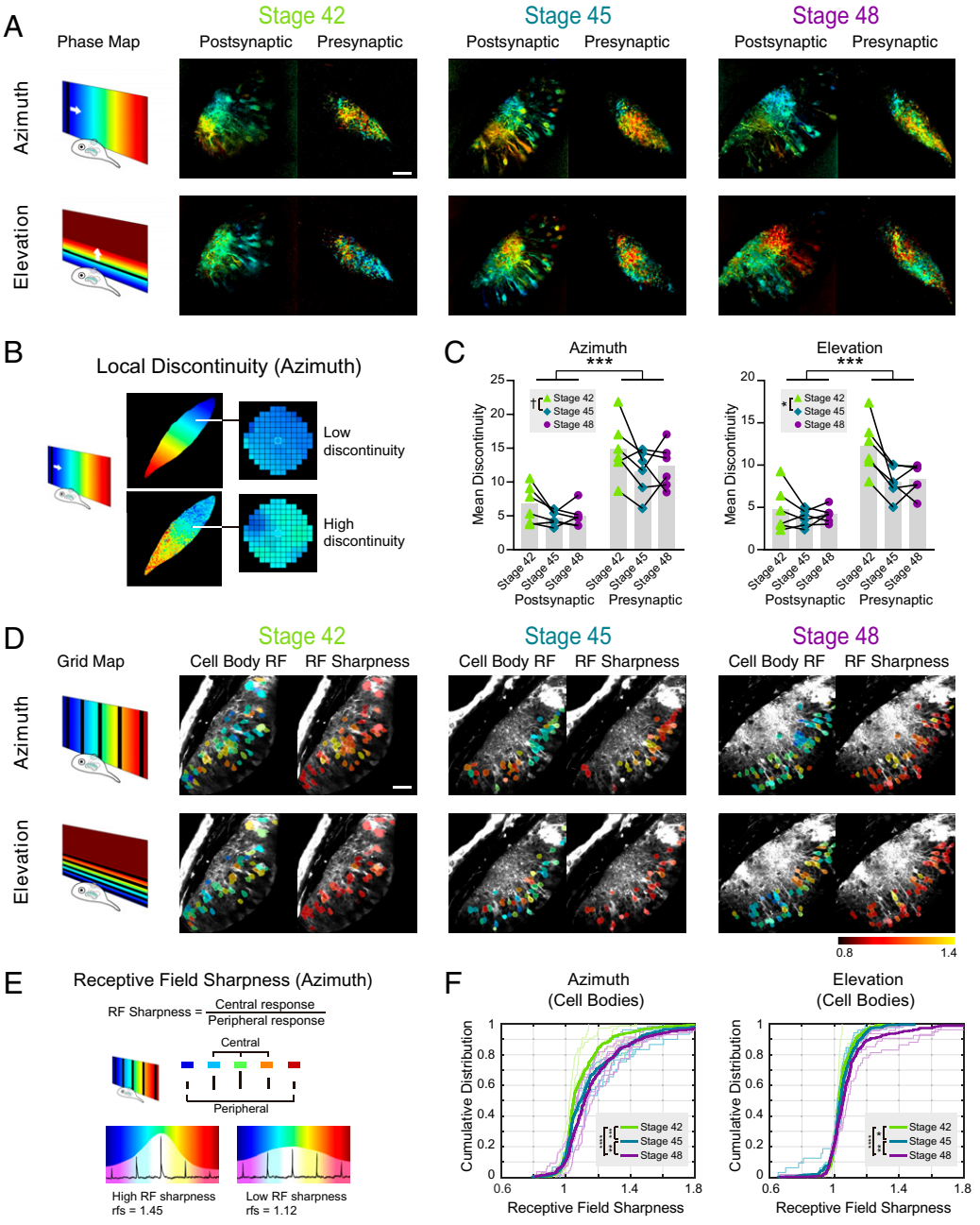

Fig. 4. Longitudinal imaging of post- and presynaptic topographic maps over development. (*A*) Post- and presynaptic phase maps extracted from the same GCaMP6s mRNA hemi-mosaic tadpole at stages 42, 45, and 48. (*B*) Local discontinuity is a measure of map smoothness. Local discontinuity for a pixel is low when the pixel is surrounded by neighboring pixels with similar phase values and high when neighboring pixels display more difference in phase. A low local discontinuity value suggests a smooth map gradient. (*C*) Mean discontinuity in tadpoles at stages 42, 45, and 48. Each data point is the mean local discontinuity for the neuropil in one animal from a single optical section ~100 μm below the top of the tectum. Linked data points are from the same animal ($n = 6$). Two-way mixed measures ANOVA for stage vs. pre/post compartment showed a significant main effect for compartment in both the azimuth and elevation axes. The main effect for stages was significant in the elevation axis and trended toward significance in the azimuth axis. Azimuth: $F_{compartment}$ (1, 10) = 34.15 (***$P = 0.0002$); F_{stages} (1.394, 13.94) = 4.059 with Greenhouse–Geisser correction ($^{\dagger}P = 0.0529$). Elevation: $F_{compartment}$ (1, 10) = 38.22 (***$P = 0.0001$); F_{stages} (1.146, 11.46) = 7.537 with Greenhouse–Geisser correction (*$P = 0.0160$). Post hoc Tukey tests showed significant differences between stages 42 and 45 in both azimuth and elevation axes: azimuth q (11) = 4.723 (*$P = 0.0167$); elevation q (11) = 4.613 (*$P = 0.0191$). (*D*) Postsynaptic cell body grid maps and cell body receptive field sharpness at stages 42, 45, and 48 from the same animal as *A*. Cell body ROIs are color coded for optimal stimulus position (left side) or RF sharpness (right side) and overlaid on an averaged postsynaptic GCaMP6s fluorescence image of the tectum. (*E*) Receptive field sharpness is an approximate measure for receptive field size. Receptive field sharpness for a pixel is low when the pixel gives similar responses to the five stimulus positions in grid mapping and high when the pixel exhibits a preference for one stimulus position. A higher receptive field sharpness value suggests a more compact receptive field. (*F*) Cumulative distribution of cell body RF sharpness at stages 42, 45, and 48. Thin lines show the cumulative distributions of tectal cell RF sharpness values from individual animals at each stage. Thick lines show the cumulative distribution of the pooled RF values for each stage (azimuth: stage 42 $n_{cells} = 337$, stage 45 $n_{cells} = 352$, stage 48 $n_{cells} = 331$; elevation: stage 42 $n_{cells} = 337$, stage 45 $n_{cells} = 351$, stage 48 $n_{cells} = 301$). Bonferroni corrected pairwise Kolmogorov–Smirnov tests were significant between the pooled results for all stages for both azimuth and elevation. Azimuth stage 42 vs. 45: ***$P = 8.92 \times 10^{-4}$; 45 vs. 48: **$P = 0.0083$; 42 vs. 48: ****$P = 1.07 \times 10^{-9}$. Elevation stage 42 vs. 45: *$P = 0.049$; stage 45 vs. 48: **$P = 0.0085$; stage 42 vs. 48: ****$P = 2.49 \times 10^{-6}$. (Scale bars: 40 μm.)

stage 42 animals (*SI Appendix*, Fig. S10) less than 24 h after the initial arrival of RGC axons in the tectum at stage 39 (19). At all stages, presynaptic maps appeared to be less well organized than the postsynaptic maps in the opposite hemisphere of the same animal, although this may have been confounded by relatively lower signal strengths in the RGC axons (*SI Appendix*, Fig. S6 *A* and *B*).

The maturation of topographic organization in the retinotectal circuit is expected to manifest both at the level of the circuit by a progressive refinement of the retinotopic gradient and at the level of individual cells through sharpening of visual receptive fields. To assess the circuit-level organization, we characterized the smoothness of the topographic gradient by measuring "local discontinuity," defined as the mean difference in receptive field (RF) position (phase) per pixel to all neighboring pixels within a 15-pixel (7.44-μm) radius. As schematized in Fig. 4*B*, a low local discontinuity value indicates a smooth local map gradient. The local discontinuity values were calculated at individual pixels (thresholded for SNR > 0.8) and then averaged across the neuropil to obtain a mean discontinuity value for the neuropil azimuth and elevation maps in each animal (*SI Appendix*, Fig. S11 *A*–*C*). The topographic organization of postsynaptic tectal maps as early as developmental stage 42 was confirmed by the fact that mean local discontinuity in stage 42 postsynaptic maps was significantly lower than that observed when the pixels were randomly scrambled within the neuropil (*SI Appendix*, Fig. S11*D*). Interestingly, for stage 42 axonal maps, only the elevation, but not azimuth, maps had lower local discontinuity than a scrambled version, suggesting that at least for the azimuthal axis, retinotectal axon arbors are initially less topographically distributed within the tectal neuropil than the synapses that they form onto their postsynaptic partners. Two-way ANOVAs revealed an effect of developmental stage on local discontinuity that was significant for elevation ($P = 0.0160$) and exhibited a trend for azimuth ($P = 0.0529$) (Fig. 4*C*). In particular, mean discontinuity was significantly lower for maps at stage 45 compared with stage 42. One caveat is that response strength and SNR also exhibited variability across stages, although these did not necessarily correspond to the changes in local discontinuity (*SI Appendix*, Fig. S6 *A* and *B*).

For both azimuth and elevation, mean discontinuity was significantly greater in presynaptic than in postsynaptic maps across all ages (azimuth: $P = 0.0002$; elevation: $P = 0.0001$). This difference in presynaptic and postsynaptic topography further supports the idea that tectal neurons can integrate and select inputs from diverse RGCs to transform responses into a more ordered topographic map.

To control for the fact that the tectum changes in size over this period of development (Fig. 2*C*), we additionally measured a normalized mean discontinuity by reducing the size of the neighborhood used to calculate local discontinuity in proportion to the different tectal neuropil areas at different stages. This normalized mean discontinuity measure also showed a significant difference between stages 42 and 45 for elevation and for pre- vs. postsynaptic maps in both axes (*SI Appendix*, Fig. S11*E*).

As the circuit becomes more precisely organized, refinement of the map is also expected to manifest at the single-cell level in the form of decreased receptive field size (22).We, therefore, evaluated "receptive field sharpness" as an approximate measure for the size of the receptive field unit (Fig. 4*D*). We defined receptive field sharpness as the average response, obtained by grid mapping, to the stimulus positions closest to the optimal stimulus position divided by the average response to the remaining stimulus positions in the periphery (Fig. 4*E*). Cumulative probability distributions of single-cell receptive field sharpness showed a progressive shift toward higher values with increasing developmental stage for both azimuth and elevation, indicating that visual response fields become more compact as the animals mature (Fig. 4*F*).

Elucidating the Effects of NMDA Receptor Blockade on Topographic Map Development. NMDA receptors are believed to play an important role in retinotectal circuit refinement (20–28). To determine the contributions of NMDA receptors to Xenopus retinotectal map refinement, tadpoles were raised with 10 μM MK-801 added to the rearing solution starting from stage 39, when RGC axons first innervate the tectum. We compared properties of retinotopic maps in these animals with control tadpoles at the same developmental stage.

Topographic maps in MK-801–treated animals imaged at stage 48 appeared qualitatively similar to maps in control animals at the same stage (Fig. 5*A*). We next quantified mean local discontinuity between control and MK-801–treated animals. For both the azimuth and elevation maps, significant main effects, but no interaction, were found by two-way independent measures ANOVA for both drug (MK-801 vs. control) and compartment (presynaptic vs. postsynaptic) (Fig. 5*B*). Moreover, no significant differences were found in response power or SNR between chronic MK-801–treated individuals and controls (*SI Appendix*, Fig. S6 *C* and *D*). These results suggest that MK-801 treatment results in coarser gradients in the topographic map. They also confirm our earlier observation in untreated animals that postsynaptic maps exhibit smoother topographic gradients than presynaptic maps (Fig. 4*C*).

Next, we evaluated receptive field sharpness for tectal cell bodies in control and MK-801–reared tadpoles. The cumulative distribution curve for azimuthal receptive field sharpness values was significantly shifted to the left for MK-801–treated animals compared with controls, indicating overall larger, less compact receptive fields (Fig. 5*C*). This result is consistent with previous reports of enlarged receptive fields resulting from chronic NMDA receptor blockade measured electrophysiologically (22). Interestingly, a comparable shift in receptive field sharpness was not seen in the elevation maps of MK-801–reared animals, despite significant differences in map discontinuity for both azimuth and elevation (Fig. 5*B*).

Because MK-801 does not wash out after binding, we performed a control experiment to exclude the possible confound of any acute effects of MK-801 on tectal calcium response and the retinotopic map. We found that MK-801 bath perfusion on stage 48 tadpoles significantly reduced the magnitude of calcium responses to our phase mapping stimulus, confirming that acutely applied MK-801 does permeate into the tadpole tectum (*SI Appendix*, Fig. S12 *A* and *B*). However, extracted phase maps did not change compared with those extracted prior to drug application in overall phase distribution and mean discontinuity (*SI Appendix*, Fig. S12 *C*–*F*). Thus, the presence of MK-801 in the medium during the imaging period alone does not affect the extracted phase maps and subsequent quantifications.

Overall, MK-801–treated animals developed retinotectal topographic maps with a coarser topographic gradient. As stage 42 maps are coarser than stage 48 maps, this result is consistent with a role for NMDA receptors in the developmental fine-tuning of topographic maps at the levels of circuit organization and single-cell input selection.

Discussion

Activity-dependent refinement of retinotopic projections, driven by patterned neuronal activity in the form of spontaneous retinal waves in amniotes (32–35) and visually evoked correlated activity in anamniotes (36, 37), is crucial for the establishment of an orderly and precise retinotopic map in the visual system. Disruption or deprivation of patterned activity has been shown to result in altered retinotopic maps in the

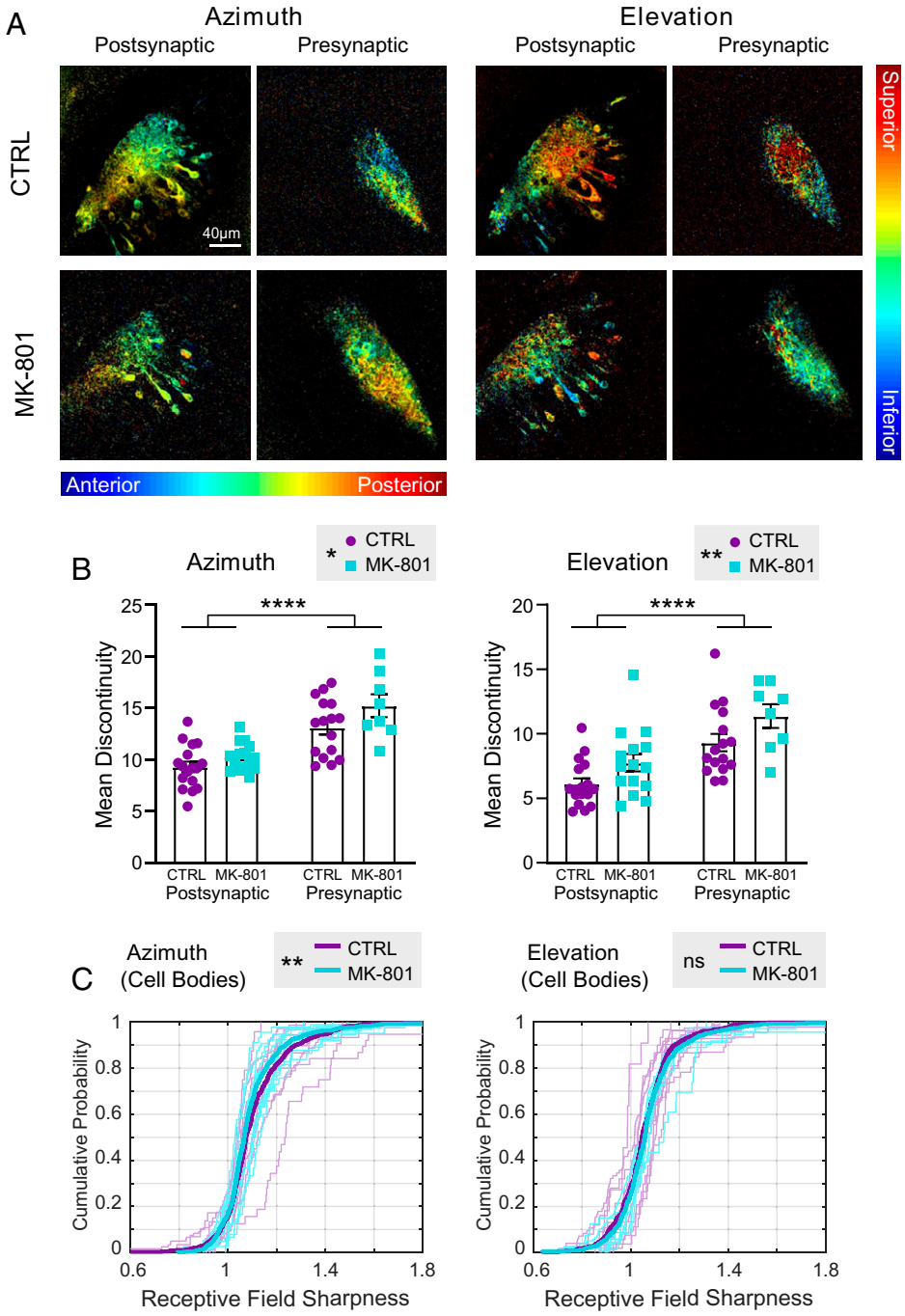

Fig. 5. GCaMP expression in post- and presynaptic compartments and effects of NMDA receptor blockade on topographic map development. (*A*) Examples of retinotopic phase maps from stage 48 animals. Starting at stage 39, animals were reared in either control medium (CTRL; *Upper*) or in medium containing 10 μM MK-801 (*Lower*). (*B*) Mean discontinuity in control vs. MK-801–reared tadpoles: presynaptic vs. postsynaptic compartments. Two-way independent measures ANOVA for drug vs. compartment shows significant main effects for both drug and compartment for both the azimuth and elevation axes. Postsynaptic: CTRL $n = 17$, MK-801 $n = 14$; presynaptic: CTRL $n = 16$, MK-801 $n = 8$. Azimuth: $F_{compartment}$ (1, 51) = 43.94 (****$P < 0.0001$); F_{drug} (1, 51) = 5.618 (*$P = 0.0216$). Elevation: $F_{compartment}$ (1, 51) = 24.29 (****$P < 0.0001$); F_{drug} (1, 51) = 7.822 (**$P = 0.0073$). (*C*) Receptive field sharpness in tectal cell bodies of control vs. MK-801–reared animals. In each plot, thin lines show the cumulative distribution of tectal cell RF sharpness values from individual CTRL and MK-801–reared animals (azimuth: CTRL $n = 8$, MK-801 $n = 10$; elevation: CTRL $n = 6$, MK-801 $n = 7$). Thick lines show the cumulative distribution of the pooled RF values for each group (azimuth CTRL $n_{cells} = 552$, MK-801 $n_{cells} = 594$; elevation CTRL $n_{cells} = 418$, MK-801 $n_{cells} = 518$). not significant (ns) for elevation, Kolmogorov–Smirnov test. **$P = 0.0016$ for azimuth.

mature animal, as demonstrated in mice with defects in spontaneous retinal waves (7, 10, 38–41). NMDA receptors are a key candidate in the processing of patterned visual activity due to their function in detecting correlated activity in converging afferents (23, 24, 26), and the disruption of NMDA receptor activity has been shown to impact morphology and response properties of individual neurons forming the topographic map (21, 22, 27, 42). Here, we pursued both a circuit- and cellular-level characterization of this phenomenon in larval Xenopus, which provides an insight into the emergence of functional retinotopic maps during the initial period of activity-dependent refinement.

In this study, we extended the previous literature of anatomical and coarse functional characterizations of topographic map refinement in the Xenopus tadpole by establishing a method to perform retinotopic mapping via in vivo two-photon calcium imaging, which allowed us to systematically visualize the developmental emergence of topographic maps across the whole tectal volume while maintaining subcellular resolution. We were able to observe fine-scale retinotopic mapping in tecta of tadpoles as young as Nieuwkoop and Faber stage 42. The noninvasive nature of this imaging method also allowed us to repeatedly image the same animals to follow the progression of the map at several subsequent developmental stages. While early electrophysiological characterizations reported large and overlapping multiunit receptive fields with no clear topographic organization before stage 46 (18), the improved spatial resolution of optical mapping methods allowed us to demonstrate that the tadpole tectum in these early stages already displays a functional topographic gradient. Receptive fields were large but displayed clear preferences for discrete stimulus positions in the visual field, consistent with later reports (19).

Comparing whole-tectum topographic gradients in the same animals at stages 45 and 48, we observed what seemed to be a Cartesian rotation in the representations of both the azimuth and elevation visual axes. This change can likely be explained in part by the growth of the tectum and addition of new tissue. The tadpole tectum expands by adding cells from a caudomedial proliferative zone, displacing existing tissue laterally and rostrally (16), which would reasonably cause a shift in the retinotopic map layout within the tectal volume. However, since presynaptic RGCs are added radially at the peripheral margin of the retina (15), one might expect the tectal map to grow increasingly distorted. Instead, we found that the azimuth and elevation axes became increasingly orthogonal to one another compared with stage 45, indicative of a more isotropic map. This observation provides evidence for the idea that presynaptic RGCs and postsynaptic tectal cells may shift their connections during development to minimize distortion of the developing retinotopic map (17, 43, 44). As these maps occupy the full volume of the tectal neuropil, fine-scale 3D analysis of developmental changes in local gradients could shed further light on the mechanisms by which the retinotopic maps shift, but the reduced axial resolution inherent in two-photon microscopy limits its precision for extracting local, rather than global, gradient orientation. A question that could, nonetheless, be raised is which circuit component leads the other in the refinement process. Do RGC axons shift their terminals to occupy newly available target space, determining the visual field representation in tectal cells, or do the receptive fields of postsynaptic tectal cells change first, after which presynaptic RGC inputs are then selected for via Hebbian plasticity? Axonal redistribution could be caused by exploratory axonal branch dynamics driven by interaxonal competition within the expanding tectum for a limited resource, such as a neurotrophic factor or postsynaptic availability (6, 8, 26, 45, 46). Additionally, because postsynaptic neurons integrate inputs from multiple converging RGCs, they could use NMDA receptors to detect correlated synaptic inputs and selectively stabilize axons that originate from neighboring RGCs in the eye through Hebbian mechanisms (8, 23).

Using single-cell mRNA blastomere injection at the two-cell stage, we were able to produce hemimorphant mosaic tadpoles expressing GCaMP6s in only one lateral half of the animal. This allowed us to separately image either the presynaptic RGCs or the postsynaptic tectal cells. We were able to visualize retinotopic maps and observed topographic gradients in both pre- and postsynaptic neuropil of stage 48 tadpoles. Applying a measurement of local discontinuity in the retinotopic representation, we found the gradient in postsynaptic neuropil to be smoother than that in the presynaptic inputs. This higher level of postsynaptic refinement preserves the possibility of a model in which the postsynaptic circuit is the driving party in the shifting projections phenomenon, first changing their retinotopic representations toward the direction of a more refined topographic gradient and then recruiting more presynaptic partners to match their receptive fields.

We used the hemimosaic GCaMP animals to investigate the effects of NMDA receptor blockade early in development on the topographic organization of the map and whether there is a differential effect in the pre- and postsynaptic circuit components. We found greater discontinuity of the topographic gradient and larger azimuthal receptive field sizes in MK-801–treated animals, consistent with previous reports (22, 27, 47, 48), adding to the evidence of NMDA receptors playing a role in activity-dependent refinement of topographic maps. An important alternative possibility, however, is that rather than freezing maps in an immature crude form, NMDA receptor blockade might actively destabilize connections and promote degradation of the map, consistent with the desegregation of ocular dominance bands seen following tectal NMDA receptor blockade in postmetamorphic three-eyed frogs (25).

Although NMDA receptor blockade altered some fine-scale properties of the topographic map, the coarse topographic gradient in the functional map remained relatively intact. Combined with our observation of map gradients at the earliest stages of tectal circuit formation, this emphasizes the extent to which the initial formation of the coarse gradient relies on molecular guidance cues instead of patterned activity (49–52). This stands in contrast with regenerating projections, which rely to a much greater extent on activity-dependent mechanisms (53). It would be interesting to apply our technique to see how NMDA receptor blockade alters the restoration of functional retinotopic gradients in regenerating projections.

The mRNA blastomere injection technique can be further expanded by performing injections into the two blastomeres at the two-cell stage, injecting GCaMP mRNA into one blastomere and a different colored calcium indicator (e.g., jRGECO1a) into the other. A coexpressed system would allow simultaneous visualization of the pre- and postsynaptic components of the same tectal circuit and not just in two hemispheres of the same animal as we have done here, permitting questions about the degree of similarity between the layout of pre- and postsynaptic map gradients to be addressed in the same structure and about whether reorganization or refinement of the topographic map in the pre- or postsynaptic component leads changes in the other.

Several factors may have impacted our ability to accurately compare receptive field properties and topographic gradients across developmental stages in young tadpoles. On one hand, the small size of the tectal neuropil at the youngest stages provides a more limited substrate in which to construct a topographic gradient. For this reason, we also repeated our measurement of local discontinuity using analysis kernels (pixel neighborhood sizes) normalized to the different tectal neuropil areas at each stage. In addition, the response strength and SNRs were considerably reduced when imaging presynaptic axons, especially in younger animals, which may have limited our sensitivity for detecting topographic gradients in the presynaptic dataset (*SI Appendix*, Fig. S6). Previous evidence has also shown that the tadpole eye is not fully developed to resolve crisp images at these stages (54), and consequently, our approach of using visually driven activity to characterize functional map organization may be limited by visual acuity of the eye, rather than fully reflecting the anatomical order of the map itself. Nonetheless, the fact that we were able to detect prominent postsynaptic azimuthal gradients in stage 42 tadpoles indicates that our assay was sufficiently sensitive to reveal information about the organization of topographic maps from the earliest stages we were able to image.

The process of circuit refinement can be thought of as a mechanism for increased wiring precision. At the single-cell level, this may take the form of greater stimulus selectivity, and in the case of retinotopy, of more compact visual receptive fields to provide the network with greater visual acuity. At the level of circuit anatomy, it often refers to spatial organization of inputs, which for retinotopy means that RGC axons come to closely recapitulate the relative layout of their somata in the eye. We examined the development of receptive field sharpness as a reflection of individual tectal cell fine-tuning. Receptive field size measurements provide an assessment of functional visual acuity at the single-cell level but offer little detail about the anatomical organization of inputs to the network. For example, it is hypothetically conceivable that a network consisting of randomly distributed neurons, each having small, defined receptive fields, might represent stimulus space precisely, but such organization would be energetically inefficient with respect to wiring conservation and not conducive to the input convergence that is needed to generate smaller receptive fields in individual cells. Therefore, we measured the degree of nearest-neighbor similarity in topographic maps with the local discontinuity measure and associated a high level of similarity with a more anatomically refined topographic map. However, the actual optimizing function used by sensory systems is yet a matter of speculation (55–57). It may, therefore, be relevant to inquire about additional properties, such as the information content stored in the retinotopic map and its capacity for decoding sensory information (58).

Overall, the present study provided an in-depth four-dimensional characterization of the emergence of functional retinotopic maps in the larval Xenopus retinotectal system and utilized this model to investigate the role of NMDA receptors in the activity-dependent refinement of the topographic map structure. This approach should serve as a valuable basis for future work on the mechanisms underlying functional retinotopic map formation.

Materials and Methods

Animals. All procedures were approved by the Animal Care Committee of the Montreal Neurological Institute at McGill University in accordance with Canadian Council on Animal Care guidelines.

Female albino *Xenopus laevis* frogs (RRID: XEP_Xla300) from our in-house breeding colony were injected with pregnant mare serum gonadotropin (Prospec) and human chorionic gonadotropin (Sigma-Aldrich) to induce ovulation, and eggs were collected for in vitro fertilization. To produce GCaMP6s transgenic tadpoles, eggs were fertilized with sperm from Xla.Tg(tubb2b:GCaMP6s)$_{NXR}$ transgenic frogs (National Xenopus Resource; RRID: NXR_0.0107). To produce tadpoles with hemilateral mosaic GCaMP6s and mCherry expression, eggs were fertilized with sperm from male albino *X. laevis* frogs; then, blastomere microinjection of GCaMP6s and mCherry mRNA to create bilateral hemimorphant animals was performed as previously described (59, 60). Briefly, a mixture of purified GCaMP6s (500 pg) and mCherry (250 pg) mRNA in 2 nL RNase-free water was pressure injected into one blastomere of two cell–stage embryos using a calibrated glass micropipette attached to a PLI-100 picoinjector (Harvard Apparatus). GCaMP and mCherry mRNA were prepared by cloning the coding sequence of GCaMP6s and mCherry into pCS2+, then linearizing plasmids with NotI, and transcribing the capped mRNA of GCaMP6s and mCherry with the SP6 mMessage mMachine Kit (Ambion; Thermo Fisher). Developing animals were screened to select individuals with hemilaterally restricted mCherry expression and high levels of GCaMP fluorescence for use in calcium imaging experiments.

All tadpoles were raised in 0.1× Modified Barth's Solution with 4-(2-hydroxyethyl)-1-piperazineethanesulfonic acid (HEPES) buffer on a 12/12-h light/dark cycle. For transgenic tadpoles, 0.001% phenylthiourea (PTU) was added to the rearing solution to reduce pigmentation. Tadpoles of both sexes were used for all studies. Tadpoles were staged according to Nieuwkoop and Faber (30).

Drugs. For NMDA receptor inhibition experiments, 10 μM MK-801 (Tocris Bioscience) was added to the tadpoles' rearing solution starting from stage 39. The rearing medium was changed, and fresh MK-801 was added every other day. Tadpoles remained in MK-801 until they were imaged at stage 48.

In Vivo Imaging and Visual Stimulation. Tadpoles were immobilized by immersion in 2 mM pancuronium bromide and immobilized in 1% low–melting point agarose in a custom chamber with a glass coverslip window on one side, through which the animal could view visual stimuli presented on an LCD screen (Fig. 1*A*). The LCD display area measured 6.5 cm (width) × 4 cm (height). The tadpole was positioned so the eye was 2.2 cm from the screen, aligned to the center of the bottom edge of the display area. From this viewpoint, the display area spans roughly 110° visual angle in azimuth and 80° in elevation. Calcium fluorescence images were captured with a high-speed resonance scanner–based two-photon microscope (Thorlabs) with piezoelectric focusing (Physik Instrumente) of a 1.0-numerical aperture 20× water immersion Nikon objective. An excitation wavelength of 910 nm was used for GCaMP6s, and emission signal was collected through a 525/50-nm bandpass filter. A #29 Wratten filter (Kodak) was installed on the LCD screen to prevent light from the display from interfering with the calcium signal. Custom MATLAB scripts based on the Psychophysics Toolbox [(61–63); RRID: SCR_002881] were used to generate the visual stimuli and synchronize stimulus presentation with image capture. Visual stimuli were presented monocularly, and calcium signal was imaged from the tectum contralateral to the stimulated eye (Fig. 1 *B* and *C*). Images (512 × 512 pixels, 0.496 μm per pixel) were collected from a single optical section at 15 Hz or from three to four optical sections (with one to two flyback frames) at 6 Hz. For full–neuropil volume mapping, two sequential sets of seven optical sections (with three flyback frames) were collected at 3 Hz with 256 × 256 pixel resolution (0.993 μm per pixel).

Receptive Field Mapping and Analysis. Processing and analyses of calcium imaging data were performed with custom scripts in MATLAB (RRID: SCR_001622) and Fiji (RRID: SCR_002285). For analyses comparing two separate recordings, images were aligned using the MATLAB *imregtform()* library function or the NoRMCorre algorithm for nonrigid motion correction (64).

Visual field representation in the tectum was then estimated with one of two methods.

Phase mapping with drifting bars. Visual stimuli consist of repeated presentations of a single vertical or horizontal 18°-wide black bar drifting at a constant rate along the full span of the anterior–posterior or superior–inferior axis. The bar width was set as a fixed on-screen pixel width that spanned an 18° visual angle on the screen position perpendicular to the eye. In some cases involving stage 42 animals, 36°-wide bar stimuli were used to produce more robust visual responses, but these were not used for quantitative analysis. Typical stimulus-triggered response to a single drifting bar shows a near-Gaussian profile, with slow onset and decay that lasts throughout the stimulus presentation (Fig. 1 *D* and *E*). Recorded images were smoothed with a two-dimensional Gaussian filter with $\sigma = 1$. The first differential was calculated for pixelwise calcium traces; then, the following analysis was applied. A Fourier transform [using MATLAB *fft()*] on a response trace converts the signal into a sum of sine waves of different frequencies, and the stimulus-evoked response can be extracted by evaluating the Fourier component at the frequency of stimulus presentation (31) (Fig. 1*F*). The amplitude of this component gives the strength of the peak stimulus–evoked response, and the phase corresponds to the time of the peak response, which converts to the bar position that evoked the response. A drifting bar continuously activates retinotectal neurons as it moves across the tectum, which results in a delay between the bar arriving at the optimal stimulus location and the time the peak response is observed. This response latency is corrected for by conducting pairs of trials where the stimulus bars sweep in opposite directions and then, taking the difference between the peak response phases to obtain an absolute response phase. For an experiment with an interval of t_{blank} between repeated drifting bar presentations, absolute phase φ^+ can be found by

$$\varphi^+ = (\varphi_1 - \varphi_2 - t_{blank})/2,$$

where φ_1 and φ_2 are the relative phases in the two opposite directions. The SNR of the response is defined as A_r/σ, where A_r is amplitude of the Fourier component at the stimulus frequency and σ is the SD of all amplitudes at frequencies above the stimulus frequency (65). This approach is justifiable because while pixels in the tectal neuropil exhibited a relatively high degree of direction selectivity on average, preferences for any given direction were homogeneously distributed across the tectum, and as a whole, the tectum did not strongly favor any one direction (*SI Appendix*, Fig. S1 *B–D*).

Grid mapping with flashing bars. Vertical or horizontal 18°-wide black bars were presented randomly at one of five set positions along the azimuth or elevation axis (numbered one to five). Each stimulus bar was flashed for 200 ms. Typical stimulus-triggered calcium signals feature a rapid (<1 s) onset

to peak and a slow decay; 15-s intervals where only the background is displayed were placed between stimulus presentations to allow the GCaMP signal to return to baseline. To extract visual field representations, the pixelwise $\Delta F/F_0$ response to each stimulus was calculated as the peak calcium signal over 1.5 s after the onset of the stimulus subtracted and divided by a baseline of the average calcium signal over 3.3 s in the blank period before the stimulus. Each pixel was then assigned an optimal stimulus position L as a weighted average:

$$L = \Sigma(L_i \times F_i)/\Sigma F_i,$$

where L_i is the bar position (one to five) and F_i is the $\Delta F/F_0$ response evoked by the bar at position L_i.

Comparing phase and grid maps from the same animal. To evaluate the consistency between retinotopic maps extracted using the two different methods, phase values from the neuropil area (thresholded for SNR > 1) were scrambled; then, both phase map and grid map position values were normalized to the mean of the scrambled phase value. We then compared phase vs. grid and phase vs. scrambled position values by averaging the absolute differences per pixel over the neuropil.

Computing cell body grid maps. Cell body ROIs were automatically segmented using Cellpose (66) and then manually processed to remove non-neuronal elements, such as melanophores and radial glia somata. $\Delta F/F_0$ responses were averaged within each ROI; then, optimal stimulus position for each ROI was calculated in same way as pixelwise optimal stimulus positions.

Global topographic gradient. The global topographic gradient was calculated from the phase maps within a volume as follows. For each pixel within the neuropil area with SNR > 1.5, a local gradient vector was calculated as the vector sum of differences in topographic position (phase) from adjacent pixels in the *x*, *y*, and *z* directions using the MATLAB function *gradient()*. All local gradient vectors within the volume were then summed and normalized to acquire the global topographic gradient.

Discontinuity. Local discontinuity was defined for a given pixel as the mean difference in receptive field position (phase) of the pixel to all neighboring pixels within a 15-pixel (7.44-μm) radius after applying an SNR > 0.8 threshold. Local discontinuity was evaluated at all pixels in the neuropil with SNR > 0.8 and with more than 30% of the pixels in its neighborhood passing SNR > 0.8. The pixelwise local discontinuity values were then averaged over the neuropil to obtain the mean discontinuity value for a given animal.

To account for the change in tectal size when comparing discontinuity in the same animal at different developmental stages, a normalized discontinuity measure was calculated by downscaling the radius of the neighborhood evaluated for each pixel. The scaled pixel radius is 15× the square root of the ratio of neuropil area at the given stage compared with stage 48, rounded to the nearest integer.

Receptive field sharpness. Maps of tectal receptive fields were derived by grid mapping. Receptive field sharpness was defined as the average $\Delta F/F_0$ response to the two stimulus positions closest to the optimal stimulus position (grid) divided by the average response to the remaining stimulus positions in the periphery. Receptive field sharpness was evaluated for cell body ROIs using average $\Delta F/F_0$ responses within the ROI. Only cell bodies with maximum stimulus response $\Delta F/F_0 > 2$ and optimal stimulus positions falling between the three central stimulus positions were evaluated. Animals with less than 30 cell bodies fitting the evaluation criteria were excluded.

Statistical Analysis. Plotted data are presented as mean ± SEM. Statistical tests, as indicated in the figures, were performed using Prism 8.0 (GraphPad software, RRID: SCR_002798).

Software Accessibility. MATLAB scripts for data analysis in this paper can be found at https://github.com/RuthazerLab/XenMap.

Data Availability. Statistical data used for this paper are included in Datasets S1–S8. Additional data generated in this study will be made available upon reasonable request. Analysis code has been deposited in GitHub (https://github.com/RuthazerLab/XenMap).

ACKNOWLEDGMENTS. We thank Dr. Amir Shmuel for providing example MATLAB code for calculating phase maps. This work was funded by a Natural Sciences and Engineering Research Council Canada Graduate Scholarship–Master's (to V.J.L.), McGill University Integrated Program in Neuroscience Studentships (to V.J.L.), Canadian Institutes of Health Research Foundation Grant FDN-143238 (to E.S.R.), and Fonds de recherche du Québec–Santé Chaire de recherche 31036 (to E.S.R.).

1. U. C. Dräger, D. H. Hubel, Topography of visual and somatosensory projections to mouse superior colliculus. *J. Neurophysiol.* **39**, 91–101 (1976).
2. R. B. Tootell, E. Switkes, M. S. Silverman, S. L. Hamilton, Functional anatomy of macaque striate cortex. II. Retinotopic organization. *J. Neurosci.* **8**, 1531–1568 (1988).
3. A. Muto, M. Ohkura, G. Abe, J. Nakai, K. Kawakami, Real-time visualization of neuronal activity during perception. *Curr. Biol.* **23**, 307–311 (2013).
4. C. M. Niell, S. J. Smith, Functional imaging reveals rapid development of visual response properties in the zebrafish tectum. *Neuron* **45**, 941–951 (2005).
5. M. Constantine-Paton, H. T. Cline, E. Debski, Patterned activity, synaptic convergence, and the NMDA receptor in developing visual pathways. *Annu. Rev. Neurosci.* **13**, 129–154 (1990).
6. T. McLaughlin, D. D. O'Leary, Molecular gradients and development of retinotopic maps. *Annu. Rev. Neurosci.* **28**, 327–355 (2005).
7. J. Cang, L. Wang, M. P. Stryker, D. A. Feldheim, Roles of ephrin-As and structured activity in the development of functional maps in the superior colliculus. *J. Neurosci.* **28**, 11015–11023 (2008).
8. E. Kutsarova, M. Munz, E. S. Ruthazer, Rules for shaping neural connections in the developing brain. *Front. Neural Circuits* **10**, 111 (2017).
9. R. O. Wong, Retinal waves and visual system development. *Annu. Rev. Neurosci.* **22**, 29–47 (1999).
10. T. McLaughlin, C. L. Torborg, M. B. Feller, D. D. M. O'Leary, Retinotopic map refinement requires spontaneous retinal waves during a brief critical period of development. *Neuron* **40**, 1147–1160 (2003).
11. S. I. Firth, C.-T. Wang, M. B. Feller, Retinal waves: Mechanisms and function in visual system development. *Cell Calcium* **37**, 425–432 (2005).
12. K. G. Pratt, M. Hiramoto, H. T. Cline, An evolutionarily conserved mechanism for activity-dependent visual circuit development. *Front. Neural Circuits* **10**, 79–79 (2016).
13. B. K. Kay, H. B. Peng, Xenopus laevis: *Practical Uses in Cell and Molecular Biology* (Academic Press, 1992).
14. C. R. Exner, H. R. Willsey, *Xenopus* leads the way: Frogs as a pioneering model to understand the human brain. *Genesis* **59**, e23405 (2021).
15. K. Straznicky, R. M. Gaze, The growth of the retina in *Xenopus laevis*: An autoradiographic study. *J. Embryol. Exp. Morphol.* **26**, 67–79 (1971).
16. K. Straznicky, R. M. Gaze, The development of the tectum in *Xenopus laevis*: An autoradiographic study. *J. Embryol. Exp. Morphol.* **28**, 87–115 (1972).
17. D. S. Sakaguchi, R. K. Murphey, Map formation in the developing *Xenopus* retinotectal system: An examination of ganglion cell terminal arborizations. *J. Neurosci.* **5**, 3228–3245 (1985).
18. R. M. Gaze, M. J. Keating, S. H. Chung, The evolution of the retinotectal map during development in *Xenopus*. *Proc. R. Soc. Lond. B Biol. Sci.* **185**, 301–330 (1974).
19. C. E. Holt, W. A. Harris, Order in the initial retinotectal map in *Xenopus*: A new technique for labelling growing nerve fibres. *Nature* **301**, 150–152 (1983).
20. L. I. Zhang, H. W. Tao, C. E. Holt, W. A. Harris, M. Poo, A critical window for cooperation and competition among developing retinotectal synapses. *Nature* **395**, 37–44 (1998).
21. I. Rajan, S. Witte, H. T. Cline, NMDA receptor activity stabilizes presynaptic retinotectal axons and postsynaptic optic tectal cell dendrites in vivo. *J. Neurobiol.* **38**, 357–368 (1999).
22. W. Dong *et al.*, Visual avoidance in *Xenopus* tadpoles is correlated with the maturation of visual responses in the optic tectum. *J. Neurophysiol.* **101**, 803–815 (2009).
23. M. Munz *et al.*, Rapid Hebbian axonal remodeling mediated by visual stimulation. *Science* **344**, 904–909 (2014).
24. M. Hiramoto, H. T. Cline, NMDARs translate sequential temporal information into spatial maps. *iScience* **23**, 101130 (2020).
25. H. T. Cline, E. A. Debski, M. Constantine-Paton, N-methyl-D-aspartate receptor antagonist desegregates eye-specific stripes. *Proc. Natl. Acad. Sci. U.S.A.* **84**, 4342–4345 (1987).
26. E. S. Ruthazer, C. J. Akerman, H. T. Cline, Control of axon branch dynamics by correlated activity in vivo. *Science* **301**, 66–70 (2003).
27. H. T. Cline, M. Constantine-Paton, NMDA receptor antagonists disrupt the retinotectal topographic map. *Neuron* **3**, 413–426 (1989).
28. D. K. Simon, G. T. Prusky, D. D. O'Leary, M. Constantine-Paton, N-methyl-D-aspartate receptor antagonists disrupt the formation of a mammalian neural map. *Proc. Natl. Acad. Sci. U.S.A.* **89**, 10593–10597 (1992).
29. T.-W. Chen *et al.*, Ultrasensitive fluorescent proteins for imaging neuronal activity. *Nature* **499**, 295–300 (2013).
30. P. Nieuwkoop, J. Faber, *Normal Table of* Xenopus laevis *(Daudin)* (Garland Publishing, New York, NY, 1994).
31. V. A. Kalatsky, M. P. Stryker, New paradigm for optical imaging: Temporally encoded maps of intrinsic signal. *Neuron* **38**, 529–545 (2003).
32. D. K. Simon, D. D. O'Leary, Development of topographic order in the mammalian retinocollicular projection. *J. Neurosci.* **12**, 1212–1232 (1992).
33. L. M. Chalupa, C. J. Snider, Topographic specificity in the retinocollicular projection of the developing ferret: An anterograde tracing study. *J. Comp. Neurol.* **392**, 35–47 (1998).
34. W. T. Wong, J. R. Sanes, R. O. Wong, Developmentally regulated spontaneous activity in the embryonic chick retina. *J. Neurosci.* **18**, 8839–8852 (1998).
35. J. B. Ackman, T. J. Burbridge, M. C. Crair, Retinal waves coordinate patterned activity throughout the developing visual system. *Nature* **490**, 219–225 (2012).
36. R. L. Vislay-Meltzer, A. R. Kampff, F. Engert, Spatiotemporal specificity of neuronal activity directs the modification of receptive fields in the developing retinotectal system. *Neuron* **50**, 101–114 (2006).

37. J. A. Demas, H. Payne, H. T. Cline, Vision drives correlated activity without patterned spontaneous activity in developing *Xenopus* retina. *Dev. Neurobiol.* **72**, 537–546 (2012).
38. M. S. Grubb, F. M. Rossi, J.-P. Changeux, I. D. Thompson, Abnormal functional organization in the dorsal lateral geniculate nucleus of mice lacking the β 2 subunit of the nicotinic acetylcholine receptor. *Neuron* **40**, 1161–1172 (2003).
39. T. D. Mrsic-Flogel *et al.*, Altered map of visual space in the superior colliculus of mice lacking early retinal waves. *J. Neurosci.* **25**, 6921–6928 (2005).
40. A. R. Chandrasekaran, R. D. Shah, M. C. Crair, Developmental homeostasis of mouse retinocollicular synapses. *J. Neurosci.* **27**, 1746–1755 (2007).
41. O. S. Dhande *et al.*, Development of single retinofugal axon arbors in normal and β2 knock-out mice. *J. Neurosci.* **31**, 3384–3399 (2011).
42. H. T. Cline, M. Constantine-Paton, NMDA receptor agonist and antagonists alter retinal ganglion cell arbor structure in the developing frog retinotectal projection. *J. Neurosci.* **10**, 1197–1216 (1990).
43. S. S. Easter Jr., C. A. Stuermer, An evaluation of the hypothesis of shifting terminals in goldfish optic tectum. *J. Neurosci.* **4**, 1052–1063 (1984).
44. T. A. Reh, M. Constantine-Paton, Retinal ganglion cell terminals change their projection sites during larval development of Rana pipiens. *J. Neurosci.* **4**, 442–457 (1984).
45. B. Alsina, T. Vu, S. Cohen-Cory, Visualizing synapse formation in arborizing optic axons in vivo: Dynamics and modulation by BDNF. *Nat. Neurosci.* **4**, 1093–1101 (2001).
46. T. N. Rahman, M. Munz, E. Kutsarova, O. M. Bilash, E. S. Ruthazer, Stentian structural plasticity in the developing visual system. *Proc. Natl. Acad. Sci. U.S.A.* **117**, 10636–10638 (2020).
47. J. T. Schmidt, M. Buzzard, R. Borress, S. Dhillon, MK801 increases retinotectal arbor size in developing zebrafish without affecting kinetics of branch elimination and addition. *J. Neurobiol.* **42**, 303–314 (2000).
48. K. A. Razak, L. Huang, S. L. Pallas, NMDA receptor blockade in the superior colliculus increases receptive field size without altering velocity and size tuning. *J. Neurophysiol.* **90**, 110–119 (2003).
49. U. Drescher *et al.*, In vitro guidance of retinal ganglion cell axons by RAGS, a 25 kDa tectal protein related to ligands for Eph receptor tyrosine kinases. *Cell* **82**, 359–370 (1995).
50. C. Brennan *et al.*, Two Eph receptor tyrosine kinase ligands control axon growth and may be involved in the creation of the retinotectal map in the zebrafish. *Development* **124**, 655–664 (1997).
51. D. A. Feldheim, D. D. M. O'Leary, Visual map development: Bidirectional signaling, bifunctional guidance molecules, and competition. *Cold Spring Harb. Perspect. Biol.* **2**, a001768 (2010).
52. V. Higenell, S. M. Han, D. A. Feldheim, F. Scalia, E. S. Ruthazer, Expression patterns of Ephs and ephrins throughout retinotectal development in *Xenopus laevis*. *Dev. Neurobiol.* **72**, 547–563 (2012).
53. J. T. Schmidt, D. L. Edwards, Activity sharpens the map during the regeneration of the retinotectal projection in goldfish. *Brain Res.* **269**, 29–39 (1983).
54. B. A. Richards, J. J. van Rheede, C. J. Akerman, Visuospatial information in the retinotectal system of *Xenopus* before correct image formation by the developing eye. *Dev. Neurobiol.* **72**, 507–519 (2012).
55. G. J. Goodhill, T. J. Sejnowski, A Unifying Objective Function for Topographic Mappings. *Neural Computation* **9**, 1291–1303 (1997).
56. M. Kaschube, Neural maps versus salt-and-pepper organization in visual cortex. *Curr. Opin. Neurobiol.* **24**, 95–102 (2014).
57. S. P. Wilson, J. A. Bednar, What, if anything, are topological maps for? *Dev. Neurobiol.* **75**, 667–681 (2015).
58. L. Avitan, Z. Pujic, N. J. Hughes, E. K. Scott, G. J. Goodhill, Limitations of neural map topography for decoding spatial information. *J. Neurosci.* **36**, 5385–5396 (2016).
59. P. Kesner, A. Schohl, E. C. Warren, F. Ma, E. S. Ruthazer, Postsynaptic and presynaptic NMDARs have distinct roles in visual circuit development. *Cell Rep.* **32**, 107955 (2020).
60. N. J. Benfey, V. J. Li, A. Schohl, E. S. Ruthazer, Sodium-calcium exchanger mediates sensory-evoked glial calcium transients in the developing retinotectal system. *Cell Rep.* **37**, 109791 (2021).
61. D. H. Brainard, The Psychophysics Toolbox. *Spatial Vis.* **10**, 433–436 (1997).
62. D. G. Pelli, The VideoToolbox software for visual psychophysics: transforming numbers into movies. *Spatial Vis.* **10**, 437–442 (1997).
63. M. Kleiner, D. Brainard, D. Pelli, What's new in Psychtoolbox-3? (2007).
64. E. A. Pnevmatikakis, A. Giovannucci, NoRMCorre: An online algorithm for piecewise rigid motion correction of calcium imaging data. *J. Neurosci. Methods* **291**, 83–94 (2017).
65. J. Warnking *et al.*, Retinotopical mapping of visual areas by fMRI using a fast cortical flattening algorithm. *Neuroimage* **11**, S646 (2000).
66. C. Stringer, T. Wang, M. Michaelos, M. Pachitariu, Cellpose: A generalist algorithm for cellular segmentation. *Nat. Methods* **18**, 100–106 (2021).

PNAS
www.pnas.org

Supplementary Information for
Topographic map formation and the effects of NMDA receptor blockade in the developing Xenopus retinotectal system

Vanessa J. Li[1], Anne Schohl[1], Edward S. Ruthazer[1]

[1]Montreal Neurological Institute-Hospital
Department of Neurology and Neurosurgery,
McGill University,
3801 Rue University,
Montréal, QC H3A 2B4, Canada

*Correspondence to: Edward S. Ruthazer
Email: edward.ruthazer@mcgill.ca

This PDF file includes:

Other supplementary materials for this manuscript include the following:

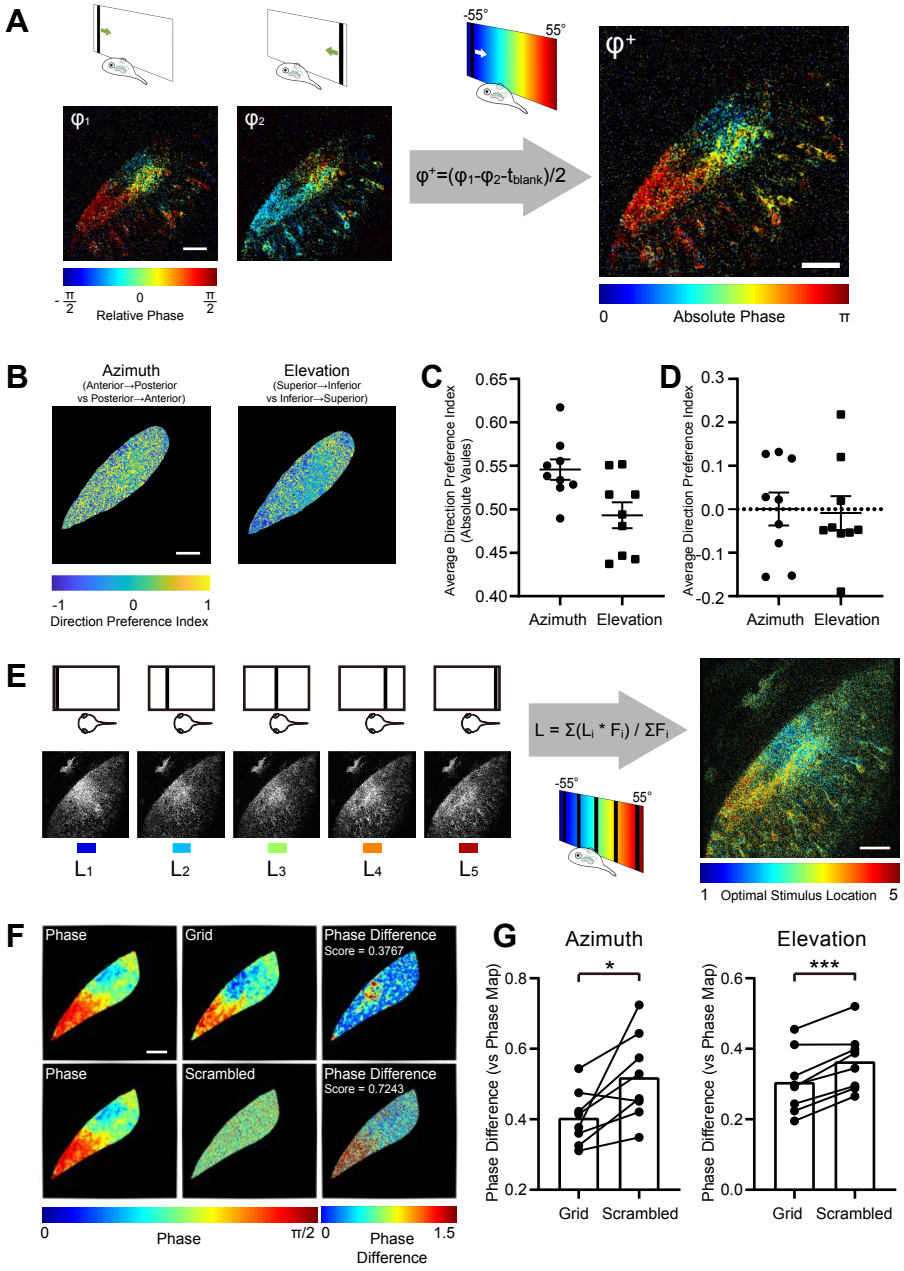
A
φ1
φ2
-55°
55°
φ+
φ+=(φ1-φ2-tblank)/2
Relative Phase
Absolute Phase
B
Azimuth
(Anterior→Posterior
vs Posterior→Anterior)
Elevation
(Superior→Inferior
vs Inferior→Superior)
Direction Preference Index
C
Average Direction Preference Index
(Absolute Values)
Azimuth
Elevation
D
Average Direction Preference Index
Azimuth
Elevation
E
L = Σ(Li * Fi) / ΣFi
L1
L2
L3
L4
L5
Optimal Stimulus Location
F
Phase
Grid
Phase Difference
Score = 0.3767
Phase
Scrambled
Phase Difference
Score = 0.7243
Phase
Phase
Difference
G
Azimuth
Elevation
Phase Difference (vs Phase Map)
Grid
Scrambled

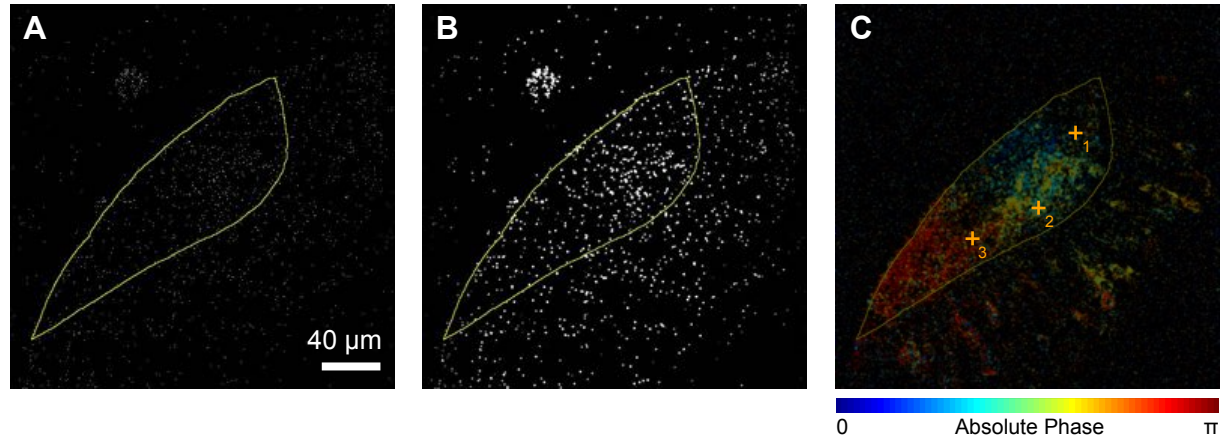
A
B
C
40 μm
1
2
3
0
Absolute Phase
π

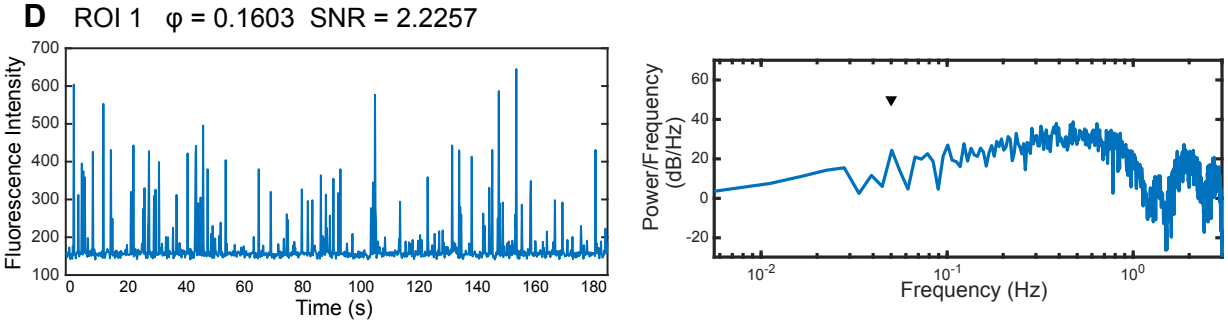
D ROI 1 φ = 0.1603 SNR = 2.2257
Fluorescence Intensity
Time (s)
Power/Frequency (dB/Hz)
Frequency (Hz)

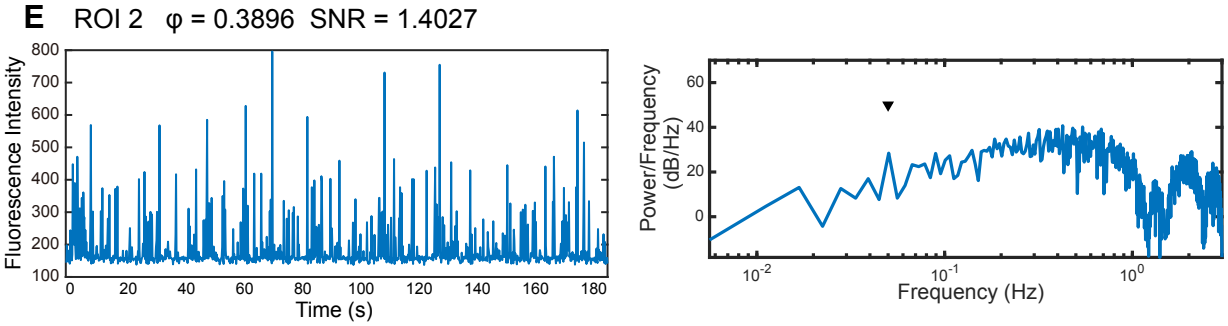
E ROI 2 φ = 0.3896 SNR = 1.4027
Fluorescence Intensity
Time (s)
Power/Frequency (dB/Hz)
Frequency (Hz)

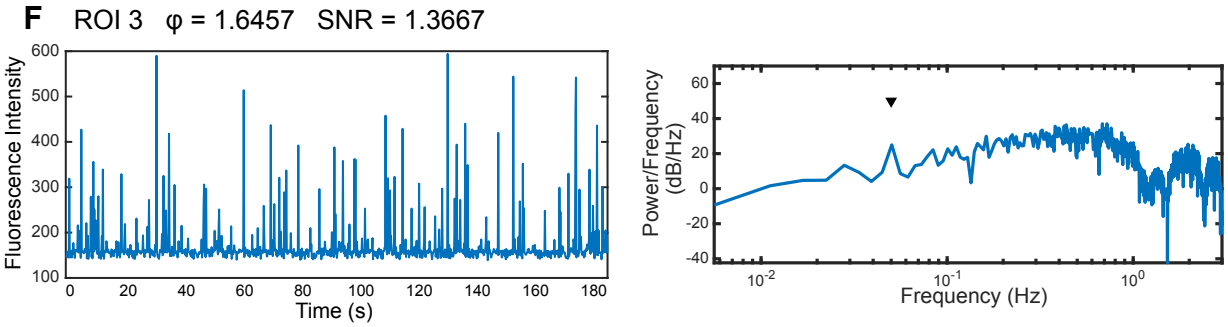
F ROI 3 φ = 1.6457 SNR = 1.3667
Fluorescence Intensity
Time (s)
Power/Frequency (dB/Hz)
Frequency (Hz)

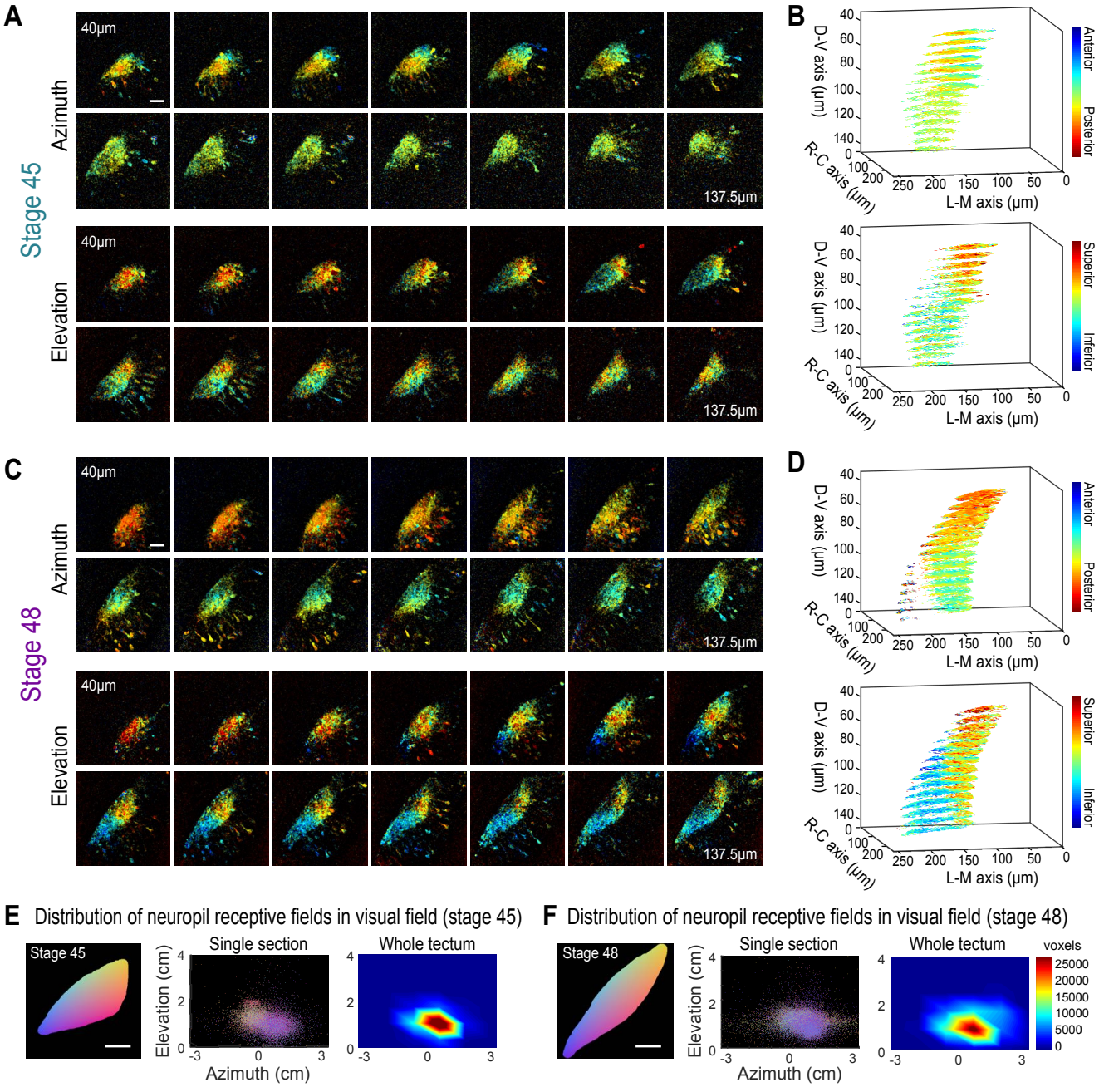
A
Stage 45
Azimuth
Elevation
40μm
137.5μm
B
D-V axis (μm)
R-C axis (μm)
L-M axis (μm)
Anterior
Posterior
Superior
Inferior
C
Stage 48
D
E Distribution of neuropil receptive fields in visual field (stage 45)
Stage 45
Single section
Whole tectum
Elevation (cm)
Azimuth (cm)
F Distribution of neuropil receptive fields in visual field (stage 48)
Stage 48
voxels
25000
20000
15000
10000
5000
0

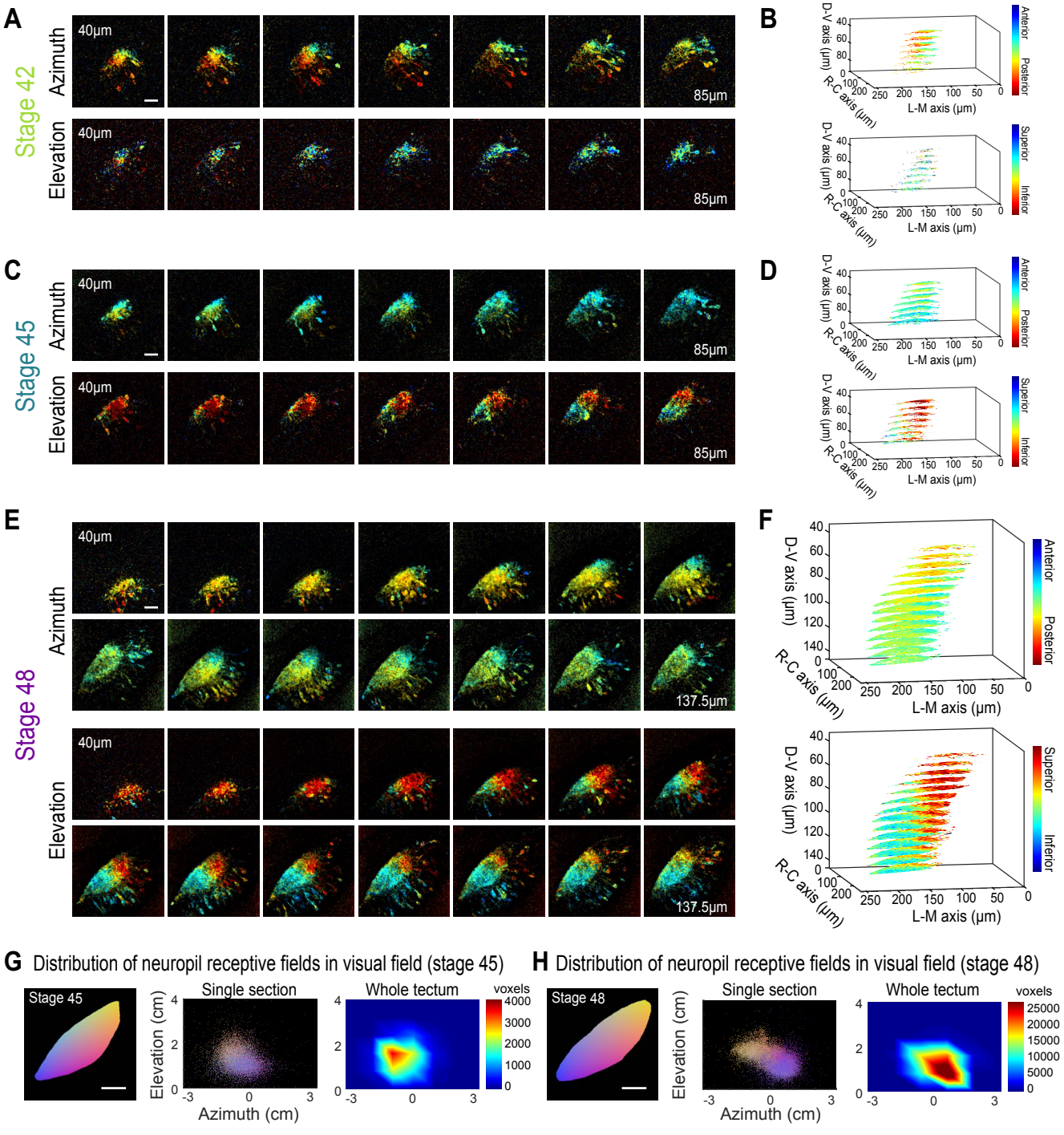
A
Stage 42
Azimuth
Elevation
40μm
85μm
B
D-V axis (μm)
R-C axis (μm)
L-M axis (μm)
Anterior
Posterior
Superior
Inferior
C
Stage 45
D
E
Stage 48
137.5μm
F
G Distribution of neuropil receptive fields in visual field (stage 45)
Stage 45
Single section
Whole tectum
voxels
Elevation (cm)
Azimuth (cm)
H Distribution of neuropil receptive fields in visual field (stage 48)
Stage 48

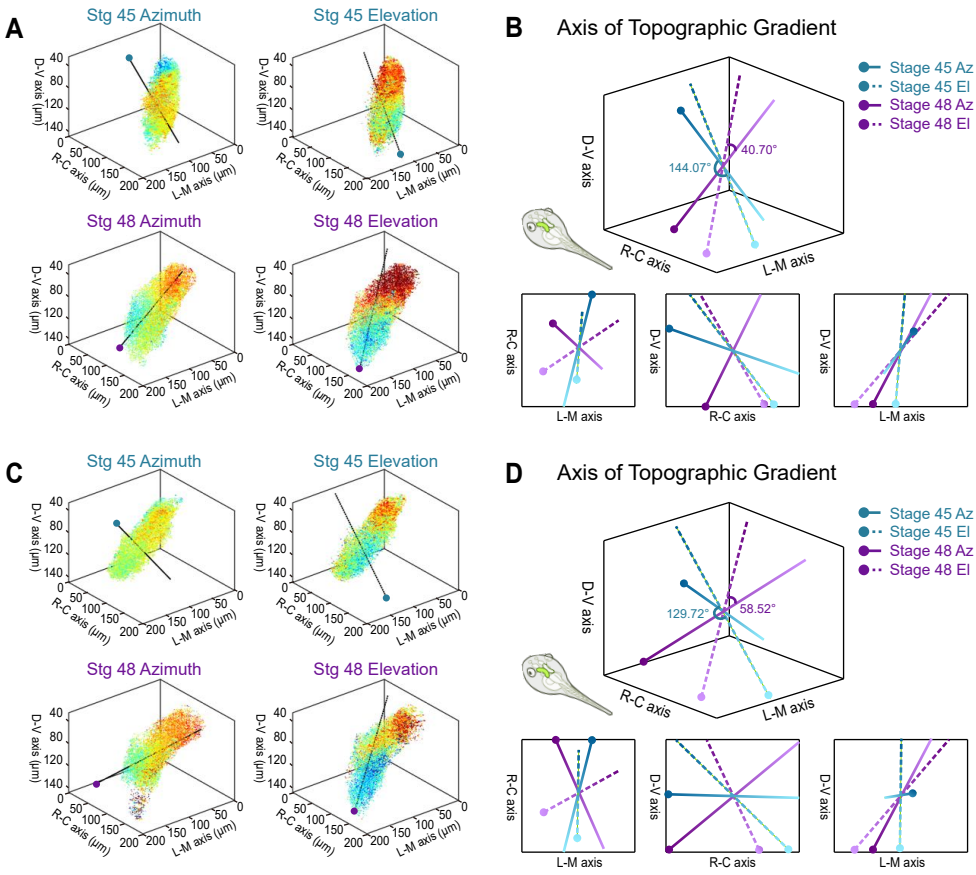
A
Stg 45 Azimuth
Stg 45 Elevation
Stg 48 Azimuth
Stg 48 Elevation
D-V axis (µm)
R-C axis (µm)
L-M axis (µm)
B
Axis of Topographic Gradient
Stage 45 Az
Stage 45 El
Stage 48 Az
Stage 48 El
144.07°
40.70°
D-V axis
R-C axis
L-M axis
C
Stg 45 Azimuth
Stg 45 Elevation
Stg 48 Azimuth
Stg 48 Elevation
D
Axis of Topographic Gradient
Stage 45 Az
Stage 45 El
Stage 48 Az
Stage 48 El
129.72°
58.52°
D-V axis
R-C axis
L-M axis

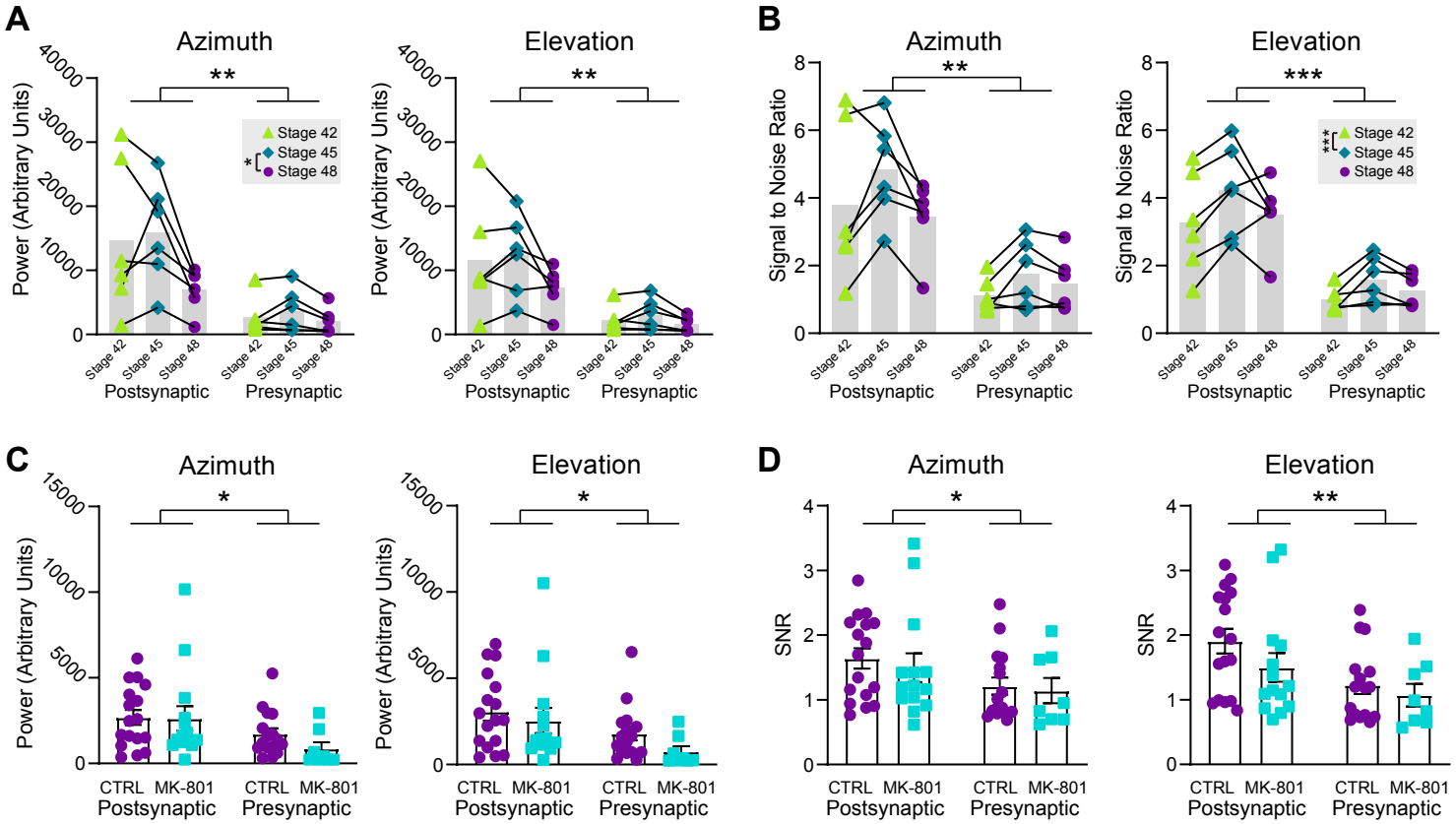
A
Azimuth
Elevation
Power (Arbitrary Units)
40000
30000
20000
10000
0
**
*
Stage 42
Stage 45
Stage 48
Stage 42
Stage 45
Stage 48
Postsynaptic
Presynaptic
B
Azimuth
Elevation
Signal to Noise Ratio
8
6
4
2
0
**
***
***
Stage 42
Stage 45
Stage 48
Postsynaptic
Presynaptic
C
Azimuth
Elevation
Power (Arbitrary Units)
15000
10000
5000
0
*
*
CTRL
MK-801
CTRL
MK-801
Postsynaptic
Presynaptic
D
Azimuth
Elevation
SNR
4
3
2
1
0
*
**
CTRL
MK-801
CTRL
MK-801
Postsynaptic
Presynaptic

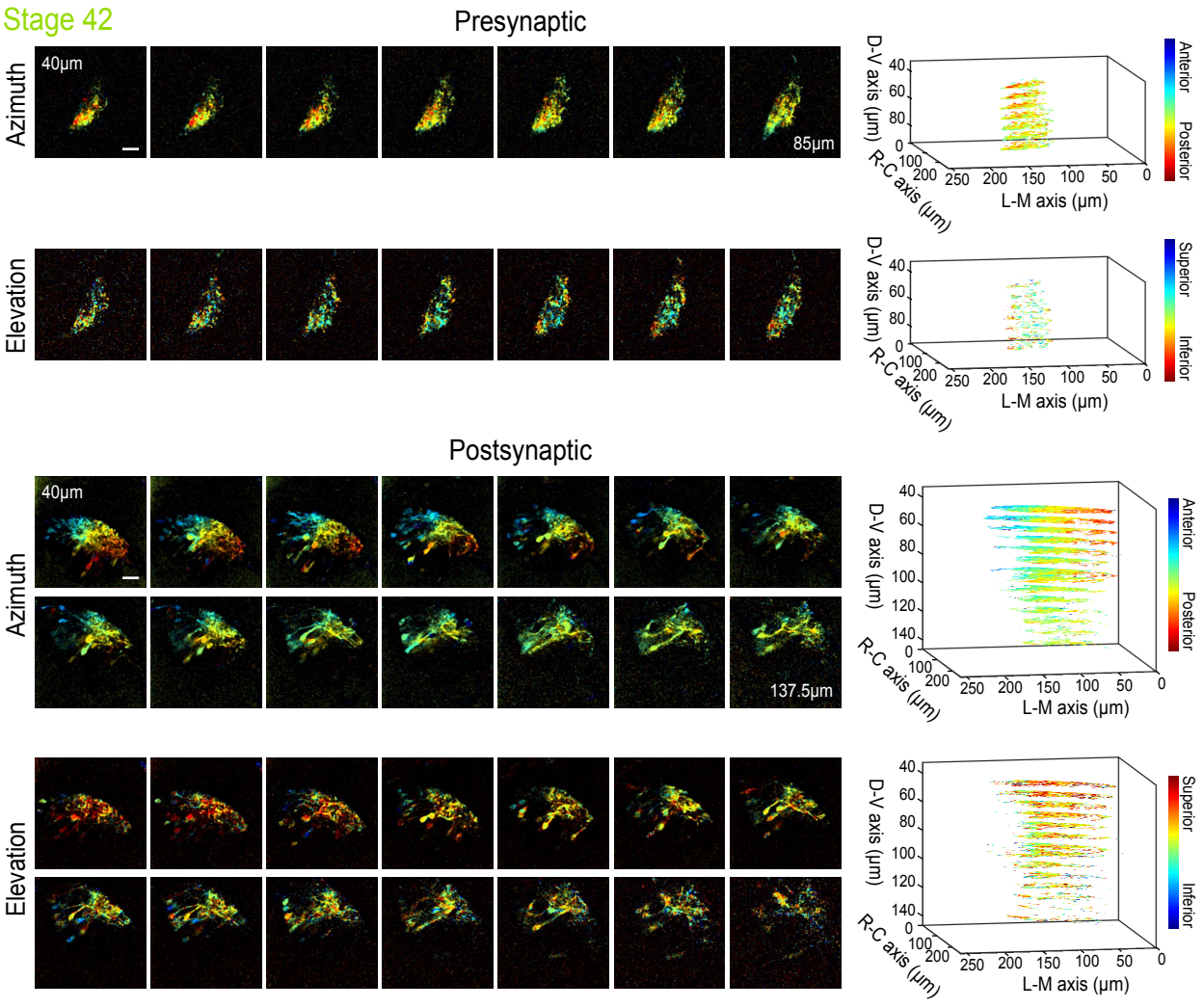
Stage 42
Presynaptic
Azimuth
40μm
85μm
Elevation
D-V axis (μm)
R-C axis (μm)
L-M axis (μm)
Anterior
Posterior
Superior
Inferior
Postsynaptic
137.5μm

Stage 45

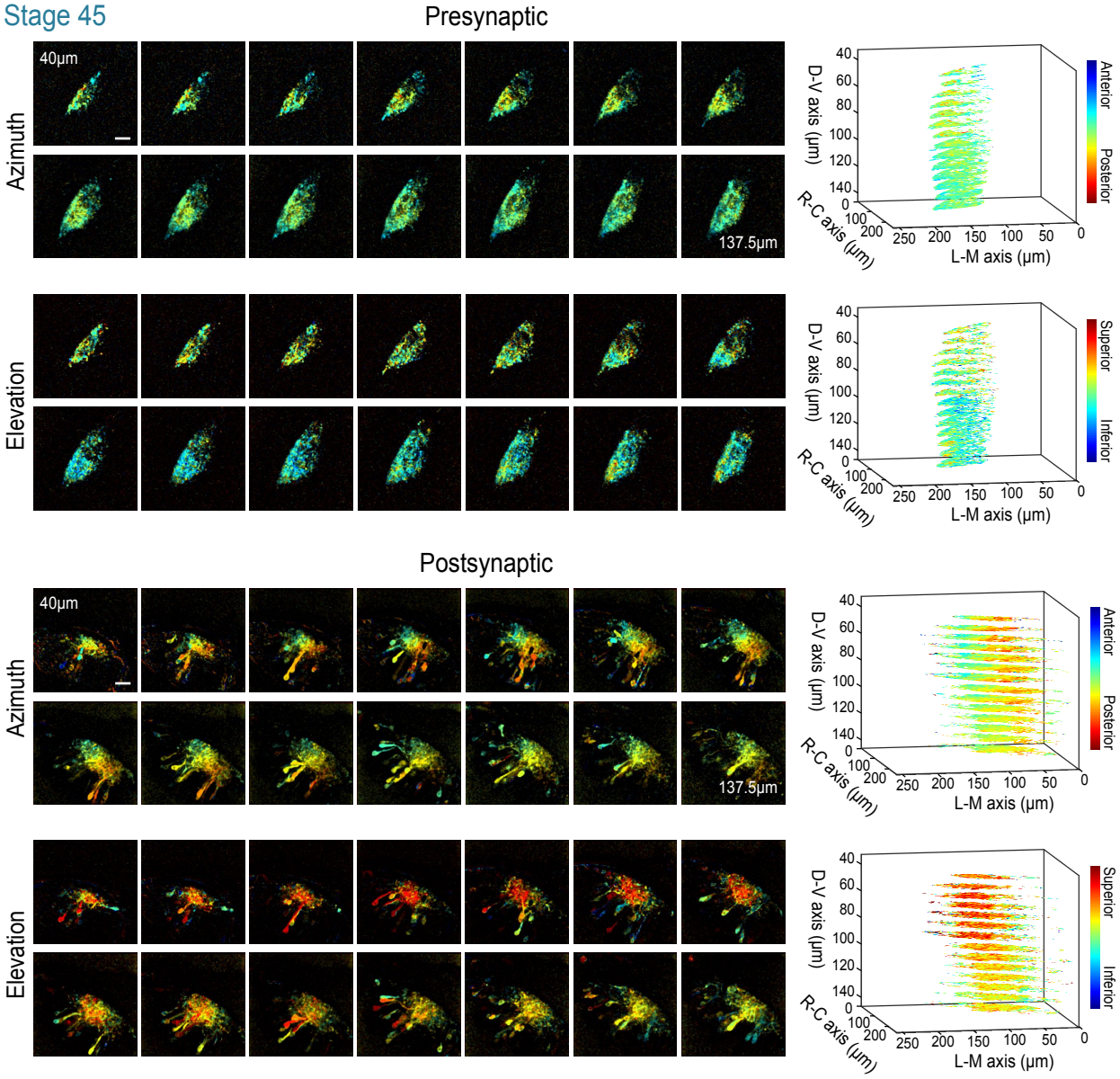
Presynaptic
Azimuth
40μm
137.5μm
Elevation
Postsynaptic
Azimuth
40μm
137.5μm
Elevation
D-V axis (μm)
R-C axis (μm)
L-M axis (μm)
Anterior
Posterior
Superior
Inferior

Stage 48

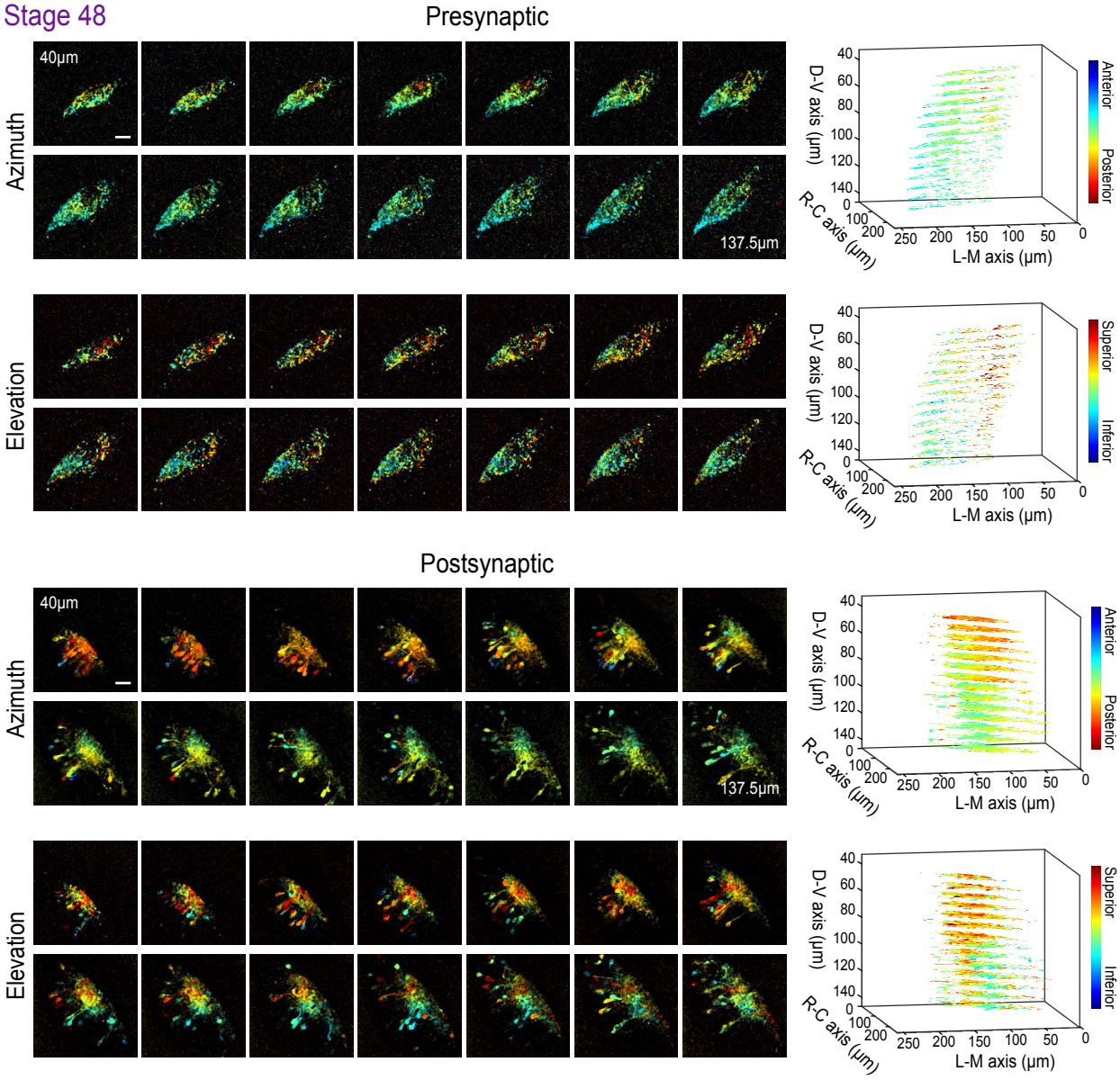
Presynaptic
Azimuth
40μm
137.5μm
Elevation
D-V axis (μm)
R-C axis (μm)
L-M axis (μm)
Anterior
Posterior
Superior
Inferior
Postsynaptic

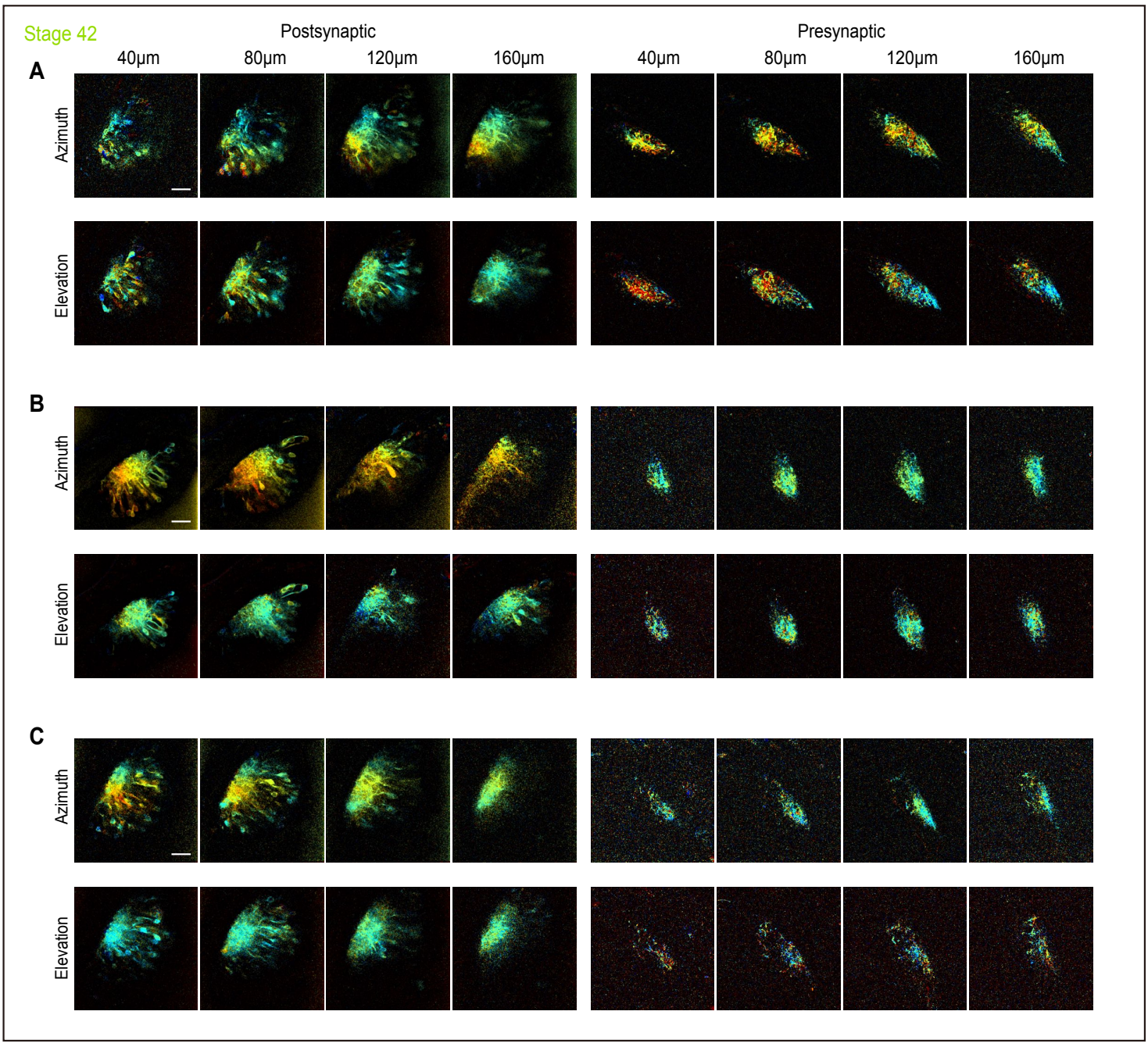
Stage 42
Postsynaptic
Presynaptic
40μm
80μm
120μm
160μm
40μm
80μm
120μm
160μm
A
Azimuth
Elevation
B
Azimuth
Elevation
C
Azimuth
Elevation

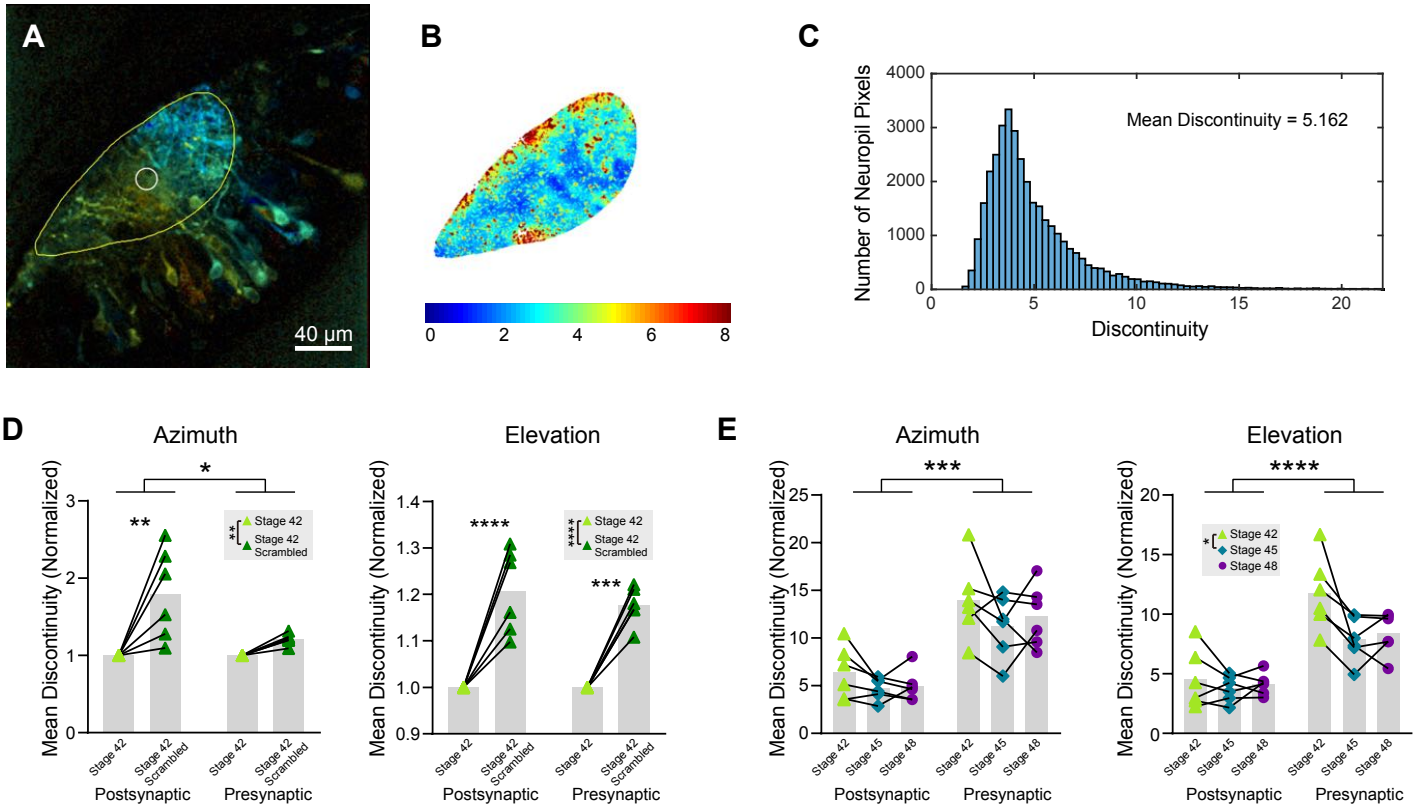
A
40 µm
B
0
2
4
6
8
C
Number of Neuropil Pixels
Mean Discontinuity = 5.162
Discontinuity
D
Azimuth
Elevation
Mean Discontinuity (Normalized)
Stage 42
Stage 42 Scrambled
Postsynaptic
Presynaptic
E
Azimuth
Elevation
Stage 42
Stage 45
Stage 48
Postsynaptic
Presynaptic

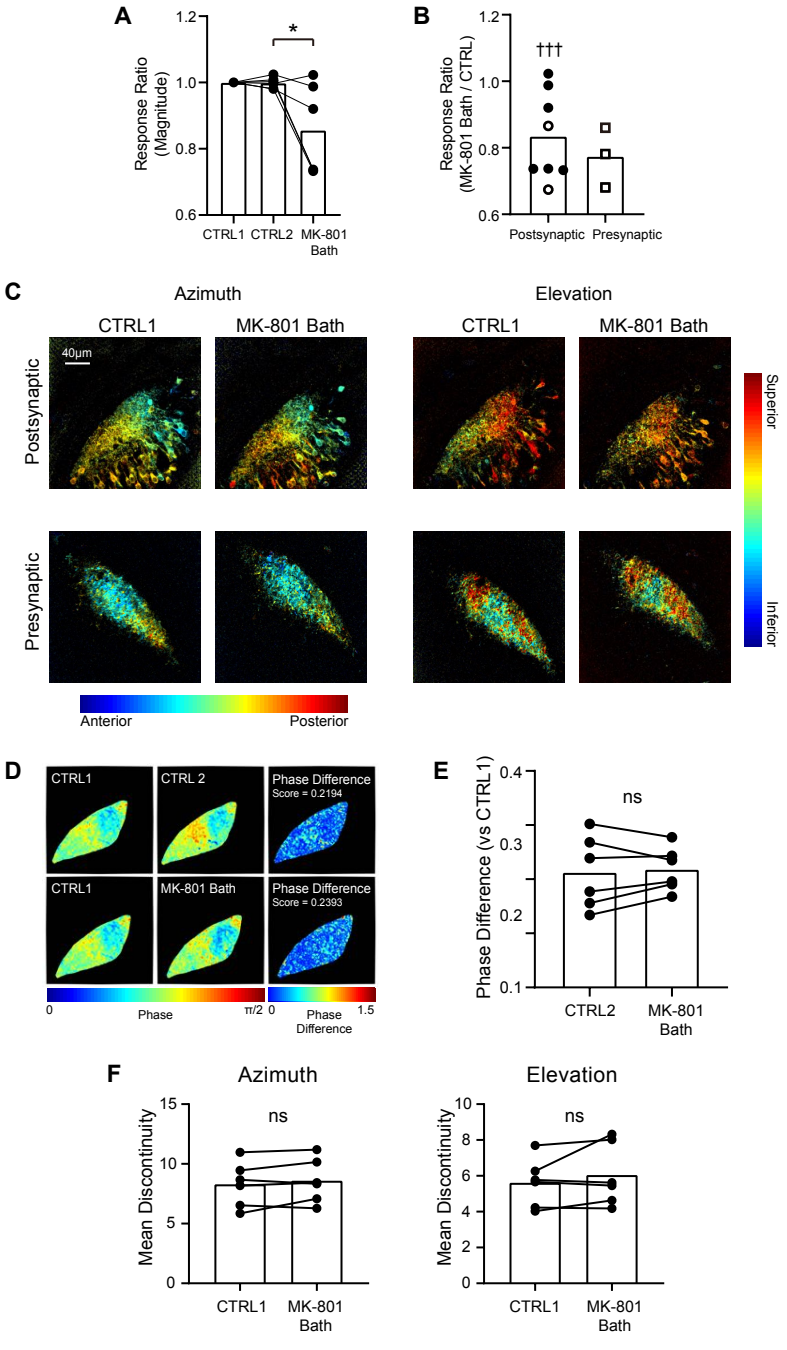
A
Response Ratio (Magnitude)
1.2
1.0
0.8
0.6
*
CTRL1
CTRL2
MK-801 Bath
B
Response Ratio (MK-801 Bath / CTRL)
†††
Postsynaptic
Presynaptic
C
Azimuth
Elevation
CTRL1
MK-801 Bath
40µm
Postsynaptic
Presynaptic
Superior
Inferior
Anterior
Posterior
D
CTRL1
CTRL 2
Phase Difference
Score = 0.2194
MK-801 Bath
Score = 0.2393
0
Phase
π/2
Phase Difference
1.5
E
Phase Difference (vs CTRL1)
0.4
0.3
0.2
0.1
ns
CTRL2
MK-801 Bath
F
Azimuth
Elevation
Mean Discontinuity
15
10
5
0
ns
CTRL1
MK-801 Bath

Supplementary Information Text

Fig. S1. Tectal response to positioned stimuli and extraction of the retinotopic map.
(A) Calculating phase maps from responses to drifting bar stimuli (azimuth). Absolute phase (φ_+) was calculated by taking the difference of phase maps extracted from opposite direction drifting bars (φ_1 and φ_2). t_{blank} represents the fixed interval between each bar sweep.

(B) Pixelwise direction preference index values in an example animal. Direction preference index is calculated as the difference between the Fourier power at the stimulation frequency for the responses evoked by opposite direction drifting bars, divided by their sum. While each pixel shows a preference for one of the two directions, pixel-wise direction preference is evenly distributed throughout the tectal neuropil.

(C) Absolute values of pixelwise direction preference index averaged over the tectal neuropil (n = 9 transgenic animals).

(D) Pixelwise direction preference index averaged over the tectal neuropil. The average direction preference indices do not significantly differ from 0 for either azimuth or elevation, indicating no overall direction preference in the neuropil (n = 9 transgenic animals, n.s. by one-sample t-test).

(E) Calculating grid maps from average tectal response to each stimulus position. Each pixel is assigned an “optimal stimulus position” as a number between 1 to 5 based on the pixel’s $\Delta F/F_0$ responses to all 5 stimulus positions, which gives an estimate of the location of the pixel’s receptive field center.

(F) Comparing phase and grid maps extracted from the same animal. A Gaussian filter with $\sigma = 3$ was applied to both the phase and grid maps, optimal stimulus position values in grid maps were converted to equivalent phase values, the two maps were aligned based on time average images, then differences between phase values in the two maps were calculated for each pixel in the neuropil and averaged to obtain a phase difference score. This score was compared to the phase difference score for the phase map compared to a scrambled version of the phase map, in which all phase values in the neuropil region were randomly shuffled.

(G) Phase difference score between phase maps, grid maps and scrambled phase maps. The phase difference score comparing phase and grid maps was significantly smaller than for phase and scrambled phase in both azimuth and elevation maps (n = 8 transgenic animals, paired t-tests, azimuth $t(7) = 2.968$, $^*p = 0.021$; elevation $t(7) = 5.947$, $^{***}p = 0.0006$).

Fig. S2. Pixel-wise analysis for phase mapping

(A) Single frame of raw calcium signal from a single 2-photon optical plane in a 3D volume in a GCaMP6s transgenic tadpole imaged at 6 Hz, responding to an anterior-to-posterior drifting bar (same animal as Fig. 1).

(B) Frame in (A) after application of a Gaussian filter with $\sigma = 1$.

(C) Absolute phase map color coded for response positions in azimuth. Pixel ROIs labelled for 3 sites.

(D) Raw calcium trace and Fourier power spectrum of its first differential at pixel ROI #1. The relative phase at the stimulus frequency is 0.1603.

(E) Raw calcium trace and Fourier power spectrum of its first differential at pixel ROI #2. The relative phase at the stimulus frequency is 0.3896.

(F) Raw calcium trace and Fourier power spectrum of its first differential at pixel ROI #3. The relative phase at the stimulus frequency is 1.6457.

Fig. S3. Retinotopic map in a transgenic tadpole (tadpole #2) at stage 45 and stage 48.

(A) Phase maps extracted from the tadpole at stage 45. Stack of 14 optical sections with 7.5 μm spacing between slices.

(B) Phase maps in A rendered as 3D volume.

(C) Phase maps extracted from the same tadpole at stage 48. Stack of 14 optical sections with

7.5 μm between slices.

(D) Phase maps in C rendered as 3D volume. In B and D, only pixels in the neuropil region with SNR > 1.5 are shown.

(E, F) Distribution of neuropil receptive fields in the visual field at (E) stage 45 and (F) stage 48. Colors represent tectal neuropil coordinates (left, middle). Density plots (right) show distribution of neuropil receptive fields from the whole tectum mapped onto the stimulus display area (summed from 14 optical sections, 7.5 μm between slices).

Fig. S4. Retinotopic map in a transgenic tadpole (tadpole #3) at stage 42, 45 and stage 48.

(A) Phase maps extracted from the tadpole at stage 42. Stack of 7 optical sections, 7.5 μm between slices.

(B) Phase maps in A rendered in 3D volume.
(C) Phase maps extracted from the same tadpole at stage 45. Stack of 7 optical sections, 7.5 μm between slices.
(D) Phase maps in C rendered in 3D volume.
(E) Phase maps extracted from the same tadpole at stage 48. Stack of 14 optical sections, 7.5 μm between slices.
(F) Phase maps in E rendered in 3D volume. In B, D and F, only pixels in the neuropil region with SNR > 1.5 are shown.
(G-H) Distribution of neuropil receptive fields in the visual field at (E) stage 45 and (F) stage 48. Colors represent tectal neuropil coordinates (left, middle). Density plots (right) show distribution of neuropil receptive fields from the whole tectum mapped onto the stimulus display area (summed from 7 optical sections at stage 45 and 14 sections at stage 48, 7.5 μm between slices).

Fig. S5. Developmental shifting of the topographic gradients at stage 45 and stage 48.

(A) 3D axes of topographic gradients at stage 45 and 48 in a transgenic tadpole (same animal as in Fig. 2). Phase maps were constructed from 14 optical sections at 7.5 μm intervals. For each optical section, 1000 random pixels in the neuropil region with SNR > 1.5 were plotted as 3D scatter points, with color indicating phase (same scales as in Fig. 2E,G). A black line in each 3D volume indicates the direction of the mean topographic (phase) gradient. The dot at the end of each line indicates the anterior direction for azimuth and inferior direction for elevation.
(B) Comparison of topographic gradient axes at stage 45 vs 48 in same animal.
(C) 3D axes of topographic gradient at stage 45 and 48 in a transgenic tadpole (same animal as in Fig. S2). Phase maps are shown in same manner as panel A.
(D) Comparison of topographic gradient axes at stage 45 vs 48, calculated from the phase maps shown in panel C.

Fig. S6. Comparison of signal strength and SNR at different developmental stages

(A) Fourier power at the stimulus frequency in response to drifting bar stimuli for GCaMP6s hemimosaic tadpoles at stages 42, 45 and 48 (n = 6 animals). Azimuth measurements were made presenting anterior-to-posterior drifting bars, and elevation with inferior to superior drifting bars. The power is calculated for pixel-wise calcium traces and averaged

over the neuropil. Two-way mixed measures ANOVA for stage vs pre/post compartment showed a significant main effect for compartment in both the azimuth and elevation axes. The main effect for stages was significant in the azimuth axis. Azimuth: $F_{compartment}$ (1, 10) = 10.23, **p = 0.0095; F_{stages} (1.362, 13.62) = 5.013 with Greenhouse-Geisser correction, *p = 0.0335. Elevation: $F_{compartment}$ (1, 10) = 11.56, **p = 0.0068; Post-hoc Tukey tests for stages in the azimuth axis showed a significant difference between stage 45 and 48, q(11) = 4.655, *p = 0.0181.

(B) Signal-to-noise ratio for the same tadpoles, calculated pixel-wise and averaged over the neuropil. Two-way mixed measures ANOVA for stage vs pre/post compartment showed a significant main effect for compartment in both the azimuth and elevation axes. The main effect for stages was significant in the elevation axis. Azimuth: $F_{compartment}$ (1, 10) = 14.88, **p = 0.0032. Elevation: $F_{compartment}$ (1, 10) = 21.47, ***p = 0.0009; F_{stages} (1.370, 13.70) = 6.402 with Greenhouse-Geisser correction, *p = 0.0175. Post-hoc Tukey tests for stages in the elevation axis showed a significant difference between stage 42 and 45, q(11) = 8.197, ***p = 0.0003.

(C) Fourier power at the stimulus frequency for control and MK-801-reared mRNA tadpoles imaged post- or presynaptically at stage 48. (Postsynaptic: CTRL n = 17, MK-801 n = 14; Presynaptic: CTRL n = 16, MK-801 n = 8.) Two-way independent measures ANOVA for drug vs compartment shows significant main effects for compartment, for both the azimuth and elevation axes. Azimuth: $F_{compartment}$ (1, 51) = 6.684, *p = 0.0126; Elevation: $F_{compartment}$ (1, 51) = 6.992, *p = 0.0109.

(D) Signal-to-noise ratio for the same tadpoles in (E), calculated pixel-wise and averaged over the neuropil. Two-way independent measures ANOVA for drug vs compartment shows significant main effects for compartment, for both the azimuth and elevation axes. Azimuth: $F_{compartment}$ (1, 51) = 4.446, *p = 0.0399; Elevation: $F_{compartment}$ (1, 51) = 7.856, **p = 0.0071.

Fig. S7. Phase maps extracted from a GCaMP6s mRNA hemimosaic tadpole at stage 42. The animal expressed GCaMP presynaptically in the left tectum, and postsynaptically in the right tectum. The maps were extracted using 36°-wide instead of 18°-wide drifting bars.

Scale bars are 40μm.

Fig. S8. **Phase maps extracted from a GCaMP6s mRNA hemimosaic tadpole at stage 45** Pre- and postsynaptic phase maps were extracted from the same animal as in Fig. S7 at stage 45. The maps were extracted using 18°-wide drifting bars.
Scale bars are 40μm.

Fig. S9. Phase maps extracted from a GCaMP6s mRNA hemimosaic tadpole at stage 48 Pre- and postsynaptic phase maps extracted from the same animal as in Figs. S7 and S8 at stage 48. The maps were extracted using 18°-wide drifting bars.
Scale bars are 40μm.

Fig. S10. Example phase maps from three GCaMP6s mRNA hemimosaic tadpoles imaged at stage 42. Stacks of 4 optical sections from 40 μm to 160 μm below the surface with 40 μm spacing between slices. For each panel (A, B, C), postsynaptic (left) and presynaptic (right) maps for the azimuth (top) and elevation (bottom) axes were collected in the same animals.
Scale bars are 40μm.

Fig. S11. Characterization of mean local discontinuity measurements.
(A) Example azimuth phase map for a stage 48 GCaMP6s mRNA tadpole (postsynaptic labelling). Pixel brightness indicates SNR. Yellow outline defines the neuropil area. White outline shows the 15-pixel (7.44 μm) radius region evaluated around a sample pixel.
(B) Scatterplot of neuropil local discontinuity values from the phase map in (A). Dark red corresponds to values greater than 8.
(C) Histogram of the discontinuity values in (B).
(D) Normalized mean discontinuity in stage 42 tadpole maps (same data as in (D)) compared to their scrambled versions (where phase values at different neuropil coordinates were randomly shuffled). Measured discontinuity values were normalized by dividing by mean discontinuity in the original map. Two-way repeated measures ANOVA for shuffling vs compartment showed a significant interaction and significant main effects for both shuffling and compartment for azimuth; and a significant main effect for shuffling for elevation. (n=6) Azimuth: $F_{interaction}(1,10) = 5.955$, *p = 0.0348; $F_{shuffling}(1,10) = 17.60$, **p = 0.0018; $F_{compartment}(1, 10) = 5.955$, *p = 0.0348; Elevation: $F_{shuffling}(1,10) = 90.49$, ****p < 0.0001. Post-hoc t-tests with Sidak correction showed stage 42 discontinuity was

significantly lower in original maps compared to scrambled in postsynaptic maps in the azimuth axis; and both pre- and postsynaptic maps in the elevation axis. Azimuth: postsynaptic $t(10) = 4.692$, $^{**}p = 0.0017$; Elevation: postsynaptic $t(10) = 7.286$, $^{****}p < 0.0001$; presynaptic $t(10) = 6.167$, $^{***}p = 0.0002$.

(E) Tectal neuropil area-normalized mean discontinuity in tadpoles at stages 42, 45 and 48. The radius of the region evaluated around each pixel was normalized between stages in proportion to the area of the neuropil. Two-way mixed measures ANOVA for stage vs compartment showed significant main effects for compartment in both azimuth and elevation axes, and a significant main effect for stage for elevation. (n=6) Azimuth: $F_{compartment}$ (1, 10) = 34.27, $^{***}p = 0.0002$; Elevation: $F_{compartment}$ (1, 10) = 39.55, $^{****}p < 0.0001$; F_{stages} (1.175, 11.75) = 6.134 with Greenhouse-Geisser correction, $^{*}p = 0.0257$. Post-hoc Tukey tests showed a significant difference in discontinuity in the elevation axis between stages 42 and 45, $q(11) = 4.180$, $^{*}p = 0.0323$.

Fig. S12. Tectal response to drifting bar stimuli after acute MK-801 application.

(A) Two sets of control phase maps were collected approximately 30 min apart, followed by application of MK-801 in the imaging chamber to achieve a final concentration of 10 μM. The Fourier power at the stimulation frequency for the 3 conditions were normalized by dividing all values by the CTRL1 measurement. Paired t-test showed a significant difference between CTRL2 and MK-801 bath ($n = 6$, $t(5) = 2.616$, $^{*}p = 0.0471$), corresponding to a 14% decrease in response magnitude following acute MK-801 application.

(B) The fractional decrease of Fourier power at the stimulation frequency in response to an anterior to posterior drifting bar after MK-801 bath application was measured for pre- and postsynaptic neuropil. Filled data points indicate data from panel (A); unfilled data points indicate data from additional animals measured without a second control recording. One-sample t-test showed a significant response magnitude decrease after MK-801 bath application in the postsynaptic neuropil ($n = 8$, $t(7) = 4.171$, $^{\dagger\dagger\dagger}p = 0.0042$).

(C) Maps extracted from drifting bar experiments before and after acute MK-801 application reveal the robustness of phase mapping to the effects of MK-801 treatment. Phase maps in each row were extracted from the same animal.

(D) Quantifying the difference between azimuth phase maps from drifting bar experiments before and after acute MK-801 application. The phase maps from CTRL2 or acute MK-

801 treatment were subtracted from CTRL1 baseline maps, and the resulting phase difference maps were averaged over the neuropil to obtain a phase difference score.
(E) Phase difference scores (versus CTRL1) for azimuth phase maps were used to compare CTRL2 vs MK-801 conditions. A paired t-test showed no significance ($n = 6$, $t(5) = 0.4812$, $p = 0.651$), indicating the maps were not different between these conditions.
(F) Tectal neuropil mean discontinuity does not change following acute MK-801 bath application. ($n = 6$, azimuth $t(5) = 1.271$, $p=0.2598$; elevation $t(5) = 1.232$, $p=0.2727$, paired t-tests).

Table S1. 3D axis gradient vectors and their angles with respect to cardinal axes

		3D Gradient Vectors			Angle with Cardinal Axes		
		x	y	z	x - mediolateral	y - rostrocaudal	z - dorsoventral
tadpole #1	45 Azimuth	79.12	315.71	147.92	77.21	27.98	65.56
	48 Azimuth	-158.52	151.43	-407.45	69.96	70.90	28.28
	45 Elevation	-8.79	-91.68	-158.66	87.25	60.02	30.13
	48 Elevation	-360.91	-241.00	-557.04	59.26	70.04	37.92
tadpole #2	45 Azimuth	44.45	187.01	10.17	76.65	13.70	86.97
	48 Azimuth	-92.36	215.07	-233.99	73.80	49.47	45.01
	45 Elevation	-2.44	-85.10	-110.38	89.00	52.38	37.64
	48 Elevation	-97.91	-53.91	-147.69	58.09	73.08	37.12

Table S1 - 3D axis gradient vectors and their angles with respect to cardinal axes.
3D azimuth and elevation gradient vectors for the data shown in Fig. S5, and their angles with respect to the cardinal axes (in degrees).

Movie S1 (separate file). Tectum calcium response to drifting bars.
Example of calcium responses to one cycle of opposite direction drifting bars (left: anterior to posterior; right: posterior to anterior). Images were acquired at 6 Hz (total 20 seconds), then a time average projection was taken for every 10 frames. The clip is looped once for better visibility of calcium response patterns.

Movie S2 (separate file). 3D azimuth phase maps of a transgenic tadpole at stage 45 and stage 48
Rotated views of the 3D azimuth phase map shown in Fig. 2E (left) and Fig. 2G (right).

Movie S3 (separate file). 3D elevation phase maps of a transgenic tadpole at stage 45 and stage 48
Rotated views of the 3D elevation phase maps shown in Fig. 2E (left) and Fig 2G. (right).

Movie S4 (separate file). 3D azimuth phase maps of a transgenic tadpole (tadpole #2) at stage 45 and stage 48
Rotated views of the 3D azimuth phase maps shown in Fig. S3B (left) and Fig. S3D (right).

Movie S5 (separate file). 3D azimuth phase maps of a transgenic tadpole (tadpole #2) at stage 45 and 48
Rotated views of the 3D elevation phase maps shown in Fig. S3B (left) and Fig. S3D (right).

Movie S6 (separate file). Presynaptic 3D azimuth phase maps of a GCaMP6s mRNA hemimosaic tadpole at stage 42, 45 and 48
Rotated views of the presynaptic 3D azimuth phase maps shown in Fig. S7 (left) S8 (middle) and S9 (right).

Movie S7 (separate file). Presynaptic 3D elevation phase maps of a GCaMP6s mRNA hemimosaic tadpole at stage 42, 45 and 48
Rotated views of the presynaptic 3D elevation phase maps shown in Fig. S7 (left) S8 (middle) and S9 (right).

Movie S8 (separate file). Postsynaptic 3D azimuth phase maps of a GCaMP6s mRNA hemimosaic tadpole at stage 42, 45 and 48

Rotated views of the postsynaptic 3D azimuth phase maps shown in Fig. S7 (left) S8 (middle) and S9 (right).

Movie S9 (separate file). Postsynaptic 3D elevation phase maps of a GCaMP6s mRNA hemimosaic tadpole at stage 42, 45 and 48

Rotated views of the postsynaptic 3D elevation phase maps shown in Fig. S7 (left) S8 (middle) and S9 (right).

Dataset S1 (separate file). Data plotted in Figure 4C

Mean discontinuity values in tadpoles at stages 42, 45 and 48 for azimuth and elevation maps of presynaptic axonal inputs and postsynaptic tectal dendritic arbors in the neuropil.

Dataset S2 (separate file). Data plotted in Figure 4F

Tab 1: Receptive field sharpness measures along the azimuth visual axis for tectal neuron somata at stages 42, 45 and 48

Tab 2: Receptive field sharpness measures along the elevation visual axis for tectal neuron somata at stages 42, 45 and 48

Dataset S3 (separate file). Data plotted in Figure 5B

Mean discontinuity values in control and MK-801-reared tadpoles, for the presynaptic (RGC axon terminals) and postsynaptic (tectal dendritic neuropil) compartments, measured independently for the azimuth and elevation axes.

Dataset S4 (separate file). Data plotted in Figure 5C

Tab 1: Receptive field sharpness measures along the azimuth visual axis for tectal neuron somata at stage 48 under control or MK-801-rearing conditions.

Tab 2: Receptive field sharpness measures along the elevation visual axis for tectal neuron somata at stage 48 under control or MK-801-rearing conditions.

Dataset S5 (separate file). Data plotted in S1 Figs C, D and G

Absolute values of pixelwise direction preference index averaged over the tectal neuropil.

Pixelwise direction preference index averaged over the tectal neuropil.

Comparison of phase and grid maps extracted from same animal.

Dataset S6 (separate file). Data plotted in S6 Figs A-D

Signal power for measurements made in hemimosaic tadpoles at stages 42, 45 and 48.

Signal-to-noise ratio for measurements made in hemimosaic tadpoles at stages 42, 45 and 48.

Signal power for measurements made in control and MK-801-reared tadpoles at stage 48.

Signal-to-noise ratio for measurements made in control and MK-801-reared tadpoles at stage 48.

Dataset S7 (separate file). Data plotted in S11 Figs D and E

Mean discontinuity in maps from stage 42 animals compared to scrambled versions of those maps. Raw and normalized datasets.

Mean discontinuity values normalized to tectum size.

Dataset S8 (separate file). Data plotted in S12 Figs A, B, E and F

Comparison of the magnitude of the signal strength at the stimulus frequency at two baseline timepoints and following acute MK-801 application. Data normalized to first baseline measurement.

Signal strength after MK-801 application relative to baseline signal for GCaMP6s expression in postsynaptic and presynaptic compartments.

Mean difference in pixelwise phase (receptive field position) compared to a baseline measurement, showing that acute MK-801-treatment does not significantly alter the map layout.

Measurements of mean local discontinuity in the same animals before and after application of MK-801 in the bath.